

Fractals made Practical: Denoising Diffusion as Partitioned Iterated Function Systems

Ann Dooms

ANN.DOOMS@VUB.BE

*Department of Mathematics & Data Science
Vrije Universiteit Brussel
Pleinlaan 2, 1050 Brussels, BELGIUM*

Abstract

What is a diffusion model actually doing when it turns noise into a photograph?

We show that the deterministic DDIM reverse chain operates as a Partitioned Iterated Function System (PIFS) and that this framework serves as a unified design language for denoising diffusion model schedules, architectures, and training objectives. From the PIFS structure we derive three computable geometric quantities: a per-step contraction threshold L_t^* , a diagonal expansion function $f_t(\lambda)$ and a global expansion threshold λ^{**} . These quantities require no model evaluation and fully characterise the denoising dynamics. They structurally explain the two-regime behaviour of diffusion models: global context assembly at high noise via diffuse cross-patch attention and fine-detail synthesis at low noise via patch-by-patch suppression release in strict variance order. Self-attention emerges as the natural primitive for PIFS contraction. The Kaplan-Yorke dimension of the PIFS attractor is determined analytically through a discrete Moran equation on the Lyapunov spectrum.

Through the study of the fractal geometry of the PIFS, we derive three optimal design criteria and show that four prominent empirical design choices (the cosine schedule offset, resolution-dependent logSNR shift, Min-SNR loss weighting, and Align Your Steps sampling) each arise as approximate solutions to our explicit geometric optimisation problems tuning theory into practice.

Keywords: Generative AI, manifold reconstruction, diffusion models, score-matching, DDIM, partitioned iterated function systems, fractal image compression, Jacobian analysis, Kaplan-Yorke dimension.

1 Introduction

Modern score-based diffusion models construct high-quality images through a sequential denoising process. The theoretical foundation lies in continuous-time stochastic differential equations (SDEs) or probability flow ODEs, which provide powerful global guarantees of distributional convergence in \mathcal{W}_2 distance (Song et al., 2021b; Ho et al., 2020). This continuous perspective is elegant, but it treats the learned score network as a black-box, giving no real structural insight in how a discrete sampling chain assembles global spatial context at early steps and synthesises localised fine detail at later ones and why is self-attention so effective as a generative primitive?

This paper answers both questions by establishing that the deterministic DDIM reverse chain Φ operates as a *Partitioned Iterated Function System* (PIFS) introduced in Jacquin (1992). We show that trained diffusion models implicitly learn such a composition to reconstruct the data manifold and that the structure of this PIFS is directly responsible for both the two-regime dynamics proved by Raya and Ambrogioni (2023) and the effectiveness of self-attention. The paper is organised around four contributions:

- **Contraction structure (Section 3).** We derive two contractivity conditions on the single-step DDIM operator Φ_t : an Euclidean condition (EC) governed by a closed-form schedule threshold L_t^* and a block-max condition (PC) that separates diagonal from cross-patch behaviour. We show that score-matching training is the diffusion analogue of Barnsley’s collage minimisation and establish an L^2 – \mathcal{W}_1 bridge quantifying how training loss controls the Wasserstein distance to the PIFS fixed point. We propose a PIFS regulariser that directly enforces (PC) during training.
- **Two-regime structure (Section 4).** The contraction study allows us to compute for each step t constants κ_t^{diag} and δ_t^{cross} from data statistics and architectural properties that structurally explain two qualitatively distinct phases of denoising. In the high- t regime (Regime I), diffuse attention drives strong cross-patch coupling while a learned directional “suppression field” $S_{k,t}$ holds every diagonal block below a so-called expansion threshold. At the highest noise levels the operator satisfies (EC) with analytically computable constants. In the low- t regime (Regime II), attention localises and suppression is released patch by patch in strict variance order, giving each release a precise geometric signature. The attention architecture is shown to control δ_t^{cross} through a bound on the softmax weights, explaining why self-attention is the natural primitive for this PIFS structure.
- **Attractor geometry (Section 5).** We characterise the fractal dimension of the PIFS attractor via its Lyapunov spectrum. Under Gaussian data, the spectrum is fully determined by the per-step diagonal expansion function $f_t(\lambda)$ from which the Kaplan-Yorke dimension of the PIFS attractor is derived. The global expansion threshold λ^{**} is the unique solution to the discrete Moran equation. The dimension of the attractor is positive if and only if the data contains at least one patch direction exceeding this threshold. For real data, the suppression field shifts the effective expansion as $f_t(\lambda_k) - S_{k,t}$, shrinking the set of expanding directions and reducing the attractor dimension.

- **Practical implications (Section 6).** The PIFS framework leads to the contraction threshold L_t^* , the per-step diagonal expansion function $f_t(\lambda)$ and the global expansion threshold λ^{**} which require no model evaluation. They constitute a design language for noise schedules and training objectives. The cosine schedule offset of Nichol and Dhariwal (2021), the resolution-dependent logSNR shift of Hoogeboom et al. (2023), Min-SNR loss weighting (Hang et al., 2023), and the Align Your Steps sampling schedule (Sabour et al., 2024) each emerge as approximate solutions to one of three explicit geometric optimisation problems identified by this language.

2 Background

2.1 Score-Based Diffusion Models

GenAI evolves around building generative models that can produce new samples from an unknown data distribution $p_{\text{data}}(x)$ on \mathbb{R}^n . The approach centres on learning the so-called score function and use it to guide a sampling process.

Definition 1 For a probability density function $p(x)$ on \mathbb{R}^n , the score function is defined as

$$s(x) := \nabla_x \log p(x) \in \mathbb{R}^n.$$

The function points in the direction of steepest increase of log-probability. If we know $s(x)$, we can generate samples from $p(x)$ using *Langevin dynamics*. Starting from an arbitrary initial point x_0 , iterate

$$x_{k+1} = x_k + \epsilon s(x_k) + \sqrt{2\epsilon} z_k, \quad z_k \sim \mathcal{N}(0, I),$$

where $\epsilon > 0$ is a step size. Under mild conditions, as $k \rightarrow \infty$ and $\epsilon \rightarrow 0$, the distribution of x_k converges to $p(x)$. This is a Markov chain Monte Carlo method.

But we do not know p_{data} , so we cannot compute its score directly. We must estimate $s(x)$ from data.

Let $\{x_0^{(i)}\}_{i=1}^N$ be i.i.d. samples from p_{data} . We wish to train a neural network $s_\theta(x)$ (with parameters θ) to approximate $\nabla_x \log p_{\text{data}}(x)$. A naive approach would minimise

$$\mathbb{E}_{p_{\text{data}}} [\|s_\theta(x_0) - \nabla_x \log p_{\text{data}}(x_0)\|^2],$$

but this requires the true score. *Score matching* Hyvärinen (2005) provides an equivalent objective that avoids the unknown density:

Theorem 2 (Score matching) If s_θ is differentiable and certain regularity conditions hold, then

$$\mathbb{E}_{p_{\text{data}}} [\|s_\theta(x_0) - \nabla_x \log p_{\text{data}}(x_0)\|^2] = \text{constant} + \mathbb{E}_{p_{\text{data}}} [\|s_\theta(x_0)\|^2 + 2\nabla_x \cdot s_\theta(x_0)].$$

The divergence term $\nabla_x \cdot s_\theta$ can be expensive in high dimensions, so alternative methods are used in practice.

Denosing Score Matching (DSM) by Vincent (2011) is a popular and tractable variant. Instead of directly targeting p_{data} , we consider a perturbed distribution. In diffusion-based

generative models, this perturbation is defined by a forward process that gradually adds noise to the data. For a sequence of timesteps $t = 1, \dots, T$, we define the noised version of a clean image x_0 as

$$x_t = \sqrt{\bar{\alpha}_t} x_0 + \sqrt{1 - \bar{\alpha}_t} \epsilon, \quad \epsilon \sim \mathcal{N}(0, I), \quad (1)$$

where $\bar{\alpha}_t = \prod_{s=1}^t \alpha_s$ is the cumulative noise schedule, strictly decreasing from $\bar{\alpha}_0 = 1$ (clean image) toward $\bar{\alpha}_T \approx 0$ (pure noise). The residual noise variance at step t is $v_t := 1 - \bar{\alpha}_t$. The specific choice of $\{\bar{\alpha}_t\}$ defines the forward process. Two widely used schedules are the *linear schedule* of Ho et al. (2020) and the *cosine schedule* of Nichol and Dhariwal (2021).

The linear schedule sets $\bar{\alpha}_t = \prod_{s=1}^t (1 - \beta_s^{\text{lin}})$ with β_s^{lin} increasing linearly from $\beta_1^{\text{lin}} = 10^{-4}$ to $\beta_T^{\text{lin}} = 0.02$. This keeps $\bar{\alpha}_t$ nearly constant at low noise (t near 1) and drops sharply near $t = T$, placing most of the signal-to-noise transition in the final steps.

The cosine schedule instead defines

$$\bar{\alpha}_t = \frac{f(t)}{f(0)}, \quad f(t) = \cos^2 \left(\frac{t/T + s_{\text{off}}}{1 + s_{\text{off}}} \cdot \frac{\pi}{2} \right), \quad (2)$$

with offset parameter $s_{\text{off}} \geq 0$; the default value $s_{\text{off}} = 0.008$ is used in practice. The offset flattens the approach of $\bar{\alpha}_t$ toward 1 near $t = 0$, preventing the schedule from decaying too rapidly at the low-noise end. The log-signal-to-noise ratio at step t is

$$\log \text{SNR}_t := \log \frac{\bar{\alpha}_t}{1 - \bar{\alpha}_t}. \quad (3)$$

We train a time-dependent network $\hat{\epsilon}_\theta(x_t, t)$ to predict the noise ϵ added to x_0 . The DSM loss becomes

$$\mathcal{L}(\theta) = \mathbb{E}_{t \sim \mathcal{U}\{1, \dots, T\}} \mathbb{E}_{x_0 \sim p_{\text{data}}} \mathbb{E}_{\epsilon \sim \mathcal{N}(0, I)} \left[\|\hat{\epsilon}_\theta(x_t, t) - \epsilon\|^2 \right],$$

where $x_t = \sqrt{\bar{\alpha}_t} x_0 + \sqrt{1 - \bar{\alpha}_t} \epsilon$. Minimising this, forces $\hat{\epsilon}_\theta(x_t, t)$ to approximate the noise that would generate x_t from x_0 . The score is then recovered via

$$\nabla_{x_t} \log p_t(x_t) \approx -\frac{\hat{\epsilon}_\theta(x_t, t)}{\sqrt{1 - \bar{\alpha}_t}}.$$

Two popular discrete-time samplers, relying on the same trained noise-prediction network $\hat{\epsilon}_\theta$, which encodes the score function across all noise levels, arise from different discretisations of these reverse dynamics.

The *stochastic sampler* from *Denoising Diffusion Probabilistic Models* (DDPM) by Ho et al. (2020) works with a Markov chain that approximates the reverse SDE. Starting from $x_T \sim \mathcal{N}(0, I)$, for $t = T, \dots, 1$ they use

$$x_{t-1} = \frac{1}{\sqrt{\alpha_t}} \left(x_t - \frac{1 - \alpha_t}{\sqrt{1 - \bar{\alpha}_t}} \hat{\epsilon}_\theta(x_t, t) \right) + \sigma_t z, \quad z \sim \mathcal{N}(0, I),$$

with σ_t typically chosen as $\sqrt{1 - \bar{\alpha}_{t-1} - \frac{1 - \bar{\alpha}_t}{\alpha_t}}$. This update corresponds to a discretisation of the reverse SDE and retains stochasticity at each step.

The *deterministic sampler* from *Denoising Diffusion Implicit Models* (DDIM) by Song et al. (2021a) works with a non-Markovian formulation that yields a deterministic generative

process. Discretising the probability flow ODE with an Euler step from t to $t - 1$ gives the DDIM update:

$$x_{t-1} = \sqrt{\bar{\alpha}_{t-1}} \hat{x}_0(x_t, t) + \sqrt{1 - \bar{\alpha}_{t-1}} \hat{\varepsilon}_\theta(x_t, t),$$

where $\hat{x}_0(x_t, t) := \frac{x_t - \sqrt{1 - \bar{\alpha}_t} \hat{\varepsilon}_\theta(x_t, t)}{\sqrt{\bar{\alpha}_t}}$ is the network's estimate of the clean image. Substituting \hat{x}_0 yields the single-step operator

$$\Phi_t(x) = \frac{\sqrt{\bar{\alpha}_{t-1}}}{\sqrt{\bar{\alpha}_t}} x + \left(\sqrt{1 - \bar{\alpha}_{t-1}} - \frac{\sqrt{\bar{\alpha}_{t-1}}}{\sqrt{\bar{\alpha}_t}} \sqrt{1 - \bar{\alpha}_t} \right) \hat{\varepsilon}_\theta(x, t) = \frac{\sqrt{\bar{\alpha}_{t-1}}}{\sqrt{\bar{\alpha}_t}} x + b_t \hat{\varepsilon}_\theta(x, t), \quad (4)$$

which uses the score (via $\hat{\varepsilon}_\theta$) to move one step backward in time and where the *score step coefficient* is given by

$$b_t := \sqrt{1 - \bar{\alpha}_{t-1}} - \frac{\sqrt{\bar{\alpha}_{t-1}} \sqrt{1 - \bar{\alpha}_t}}{\sqrt{\bar{\alpha}_t}}. \quad (5)$$

Because no noise is added, the process defines a deterministic mapping $x_T \mapsto x_0 = \Phi(x_T)$ and can be run with fewer steps by sub-sampling the timesteps. This sampler will be the object of our study.

Proposition 3 (Sign of b_t) *For any strictly decreasing $\{\bar{\alpha}_t\}$ with $\bar{\alpha}_0 = 1$, $b_t < 0$ for all $t \geq 1$.*

Proof $b_t < 0 \iff \sqrt{1 - \bar{\alpha}_{t-1}} < \sqrt{\bar{\alpha}_{t-1}} \sqrt{1 - \bar{\alpha}_t} / \sqrt{\bar{\alpha}_t}$, which is true as the schedule is strictly decreasing. \blacksquare

Because the sampler is deterministic, the full reverse chain defines a *deterministic map* $\Phi = \Phi_1 \circ \dots \circ \Phi_T : \mathbb{R}^n \rightarrow \mathbb{R}^n$ from noise to image, each Φ_t with distinct parameters $\bar{\alpha}_t$ and b_t and distinct score-network behaviour at each noise level. The trained network $\hat{\varepsilon}_\theta$ approximates the *optimal predictor* $\varepsilon_\theta^*(x_t, t) := -\sqrt{v_t} \nabla_{x_t} \log p_t(x_t)$, the true score of the noised marginal p_t .

The central observation motivating the PIFS connection is that each Φ_t in (4) has two competing effects: the factor $\sqrt{\bar{\alpha}_{t-1}}/\sqrt{\bar{\alpha}_t} > 1$ expands distances, while $b_t < 0$ counteracts this expansion through the score correction. Whether the net effect is contractive depends on how strongly the score Jacobian drives the system inward.

2.2 Partitioned Iterated Function Systems

Recall that a map $w : (X, d) \rightarrow (X, d)$ is a *contraction* if $d(w(x), w(y)) \leq s d(x, y)$ for some $s \in [0, 1)$, called *contraction factor*, and all $x, y \in X$.

Theorem 4 (Banach Fixed Point Theorem (Banach, 1922)) *Let (X, d) be a complete metric space and w a contraction with factor $s < 1$. There exists a unique $x^* \in X$ with $w(x^*) = x^*$ and $\lim_{k \rightarrow \infty} w^k(x) = x^*$ for all $x \in X$, at rate $d(w^k(x), x^*) \leq s^k d(x, x^*)$.*

An *iterated function system* (IFS) $\{w_k\}_{k=1}^N$ consists of contractions on (X, d) . The *Hutchinson operator* $\mathcal{H}(A) = \bigcup_k w_k(A)$ is itself a contraction on $(\mathcal{C}(\mathbb{R}^2), d_H)$, the complete space of non-empty compact subsets of \mathbb{R}^2 equipped with the Hausdorff metric d_H . It hence has a unique fixed point attractor A^* reached by iterating from any starting compact set (Hutchinson, 1981). This operator was the theoretical basis for fractal image compression.

Theorem 5 (Collage Theorem (Barnsley, 1988)) *For every compact set A*

$$d_H(A, A^*) \leq \frac{1}{1-s} d_H(A, \mathcal{H}(A)), \quad (6)$$

Indeed, by Barnsley’s theorem we have that whenever A is close in Hausdorff distance to its image under the operator \mathcal{H} , the distance between A and the attractor of \mathcal{H} is smaller than the distance to its “collage” of smaller copies of itself, the *collage error*. This is applicable to sets with *global self-similarity*, like fractals for which the collage error is zero. Global self-similar compact sets A can hence be *reconstructed* from any other compact set by iterating an IFS consisting of contractions describing the smaller copies for which the Hutchinson operator minimises the distance to $\mathcal{H}(A)$.

Natural images, however, do not exhibit the global self-similarity as different regions of an image are typically unrelated, so a single IFS cannot represent them accurately. (Jacquin, 1992) showed that this limitation can be overcome by extending the Collage Theorem to a *Partitioned IFS* (PIFS) $\{w_k\}_{k=1}^N$, which works at patch level as natural images exhibit local self-similarity. Indeed, parts of an image look like other parts after shrinking combined with operations like rotations, reflections and translations.

For a PIFS, the image is partitioned into non-overlapping patches called *range blocks* $\{R_k\}_{k=1}^M$ (the output tiles to be encoded) and a set of larger *domain blocks* $\{D_j\}$ (candidate source tiles, drawn from a pool that covers the image). Each range block R_k is encoded by an affine map

$$w_k(x) = s_k A_k(\text{DS}(D_{j(k)})) + o_k,$$

where DS is a spatial downsampling operator that matches domain and range block sizes, A_k is a geometric symmetry (rotation or reflection), $s_k \in [0, 1]$ is a luminance scaling factor enforcing contractivity, and o_k is a luminance offset. The encoder searches over the pool of domain blocks and a discrete set of symmetries to find, for each range block, the $(j(k), A_k, s_k, o_k)$ minimising the Euclidean distance between $w_k(D_{j(k)})$ and R_k , called the *collage error at the block level*. The collection $\{w_k\}_{k=1}^N$ defines a PIFS whose attractor, reached by iterating the system from any initial image approximates the original. Contractivity is guaranteed per block rather than globally, enabling the system to capture local texture repetition while allowing global structure to vary across blocks.

3 Contraction Structure of the Denoising Operator

Asking whether the deterministic DDIM reverse chain $\Phi = \Phi_1 \circ \dots \circ \Phi_T$ is a PIFS means investigating whether it is contractive on patch-level. As the operator is a composition of denoising steps, we will first concentrate on the Φ_t .

The operator Φ_t is a contraction in $(\mathbb{R}^n, \|\cdot\|_2)$ if and only if $\|J_x \Phi_t\|_{\text{op}} < 1$ for all x , where $J_x \Phi_t(x) := \nabla_x \Phi_t(x) \in \mathbb{R}^{n \times n}$ is the *Jacobian*. Recall that for a linear operator A , $\|A\|_{\text{op}} := \sup_{\|x\|_2=1} \|A(x)\|_2$ denotes the *operator norm*, which equals the largest singular value of its matrix. Differentiating (4) with respect to x gives

$$J_x \Phi_t(x) = \frac{\sqrt{\bar{\alpha}_{t-1}}}{\sqrt{\bar{\alpha}_t}} I + b_t J_x \hat{\varepsilon}_\theta(x, t), \quad (7)$$

so the Jacobian of the denoising operator decomposes as a scaled identity plus a correction term entirely determined by the score network's Jacobian $J_x \hat{\varepsilon}_\theta$. Every contractivity question about Φ_t therefore relates to an algebraic condition on $J_x \hat{\varepsilon}_\theta$.

3.1 Contraction in the Euclidean Norm

Because of the Jacobian formula (7), Φ_t is contractive when

$$\left\| \frac{\sqrt{\bar{\alpha}_{t-1}}}{\sqrt{\bar{\alpha}_t}} I + b_t J_x \hat{\varepsilon}_\theta(x, t) \right\|_{\text{op}} < 1. \quad (8)$$

Theorem 6 (Euclidean Contraction) *Let $\hat{\varepsilon}_\theta(\cdot, t) : \mathbb{R}^n \rightarrow \mathbb{R}^n$ be C^1 , and suppose its Jacobian admits, for every $x \in \mathbb{R}^n$, the decomposition*

$$J_x \hat{\varepsilon}_\theta(x, t) = \nu_t(x) I_n + R_t(x), \quad (9)$$

where $\nu_t : \mathbb{R}^n \rightarrow (0, \infty)$ is a positive scalar field, I_n is the $n \times n$ identity, and the residual $R_t(x) \in \mathbb{R}^{n \times n}$ satisfies $\|R_t\|_{\text{op}} \leq \delta_t$. Define the contraction threshold

$$L_t^* := \frac{\sqrt{\bar{\alpha}_{t-1}/\bar{\alpha}_t} - 1}{|b_t|} > 0, \quad (10)$$

and set $\nu_t^{\min} := \inf_{x \in \mathbb{R}^n} \nu_t(x)$. Assume:

$$(C1) \quad \nu_t^{\min} > L_t^* + \delta_t, \quad (11)$$

$$(C2) \quad |b_t| \nu_t(x) \leq \frac{\sqrt{\bar{\alpha}_{t-1}}}{\sqrt{\bar{\alpha}_t}} \quad \text{for all } x \in \mathbb{R}^n. \quad (12)$$

Then $\Phi_t : \mathbb{R}^n \rightarrow \mathbb{R}^n$ is a contraction in $(\mathbb{R}^n, \|\cdot\|_2)$ with contraction factor

$$\kappa_t := 1 - |b_t|(\nu_t^{\min} - L_t^* - \delta_t) \in (0, 1). \quad (13)$$

Proof Substituting (9) into (7) gives

$$J_x \Phi_t = c(x) I_n + b_t R_t(x), \quad c(x) := \frac{\sqrt{\bar{\alpha}_{t-1}}}{\sqrt{\bar{\alpha}_t}} + b_t \nu_t(x). \quad (14)$$

Since $b_t < 0$, condition (C2) reads $-b_t \nu_t(x) \leq \frac{\sqrt{\bar{\alpha}_{t-1}}}{\sqrt{\bar{\alpha}_t}}$, hence $c(x) \geq 0$.

As $\nu_t(x) \geq \nu_t^{\min}$, the scalar $c(x)$ is decreasing in $\nu_t(x)$, so

$$c(x) \leq \frac{\sqrt{\bar{\alpha}_{t-1}}}{\sqrt{\bar{\alpha}_t}} - |b_t| \nu_t^{\min} = \kappa_t - |b_t| \delta_t.$$

The triangle inequality applied to $J_x\Phi_t = c(x)I_n + b_tR_t(x)$ gives

$$\|J_x\Phi_t\|_{\text{op}} \leq c(x) + |b_t|\|R_t\|_{\text{op}} \leq c(x) + |b_t|\delta_t \leq \kappa_t.$$

Condition (C1) gives $\kappa_t < 1$; condition (C2) and $\nu_t^{\min} - L_t^* - \delta_t > 0$ give $\kappa_t > 0$. We then get that $\|\Phi_t(x) - \Phi_t(y)\|_2 \leq \kappa_t\|x - y\|_2$ for all $x, y \in \mathbb{R}^n$. \blacksquare

Definition 7 ((EC): Euclidean Contraction) Φ_t satisfies (EC) if $\hat{\varepsilon}_\theta(\cdot, t)$ is C^1 , its Jacobian admits decomposition (9) for all $x \in \mathbb{R}^n$, and the constants (ν_t^{\min}, δ_t) satisfy conditions (C1) and (C2).

(EC) is hence a condition on the score network, where its two constants ν_t^{\min} and δ_t can be derived from the score Jacobian, while the threshold L_t^* is determined entirely by the noise schedule and carries no dependence on the network or the data. Hence Φ_t is an Euclidean contraction whenever (EC) holds. The contraction factor κ_t (13) makes the dependence on the score network explicit.

Corollary 8 Suppose (EC) holds for every Φ_t ($t \in \{1, \dots, T\}$) with respective factors $\kappa_t \in (0, 1)$. Then the composition $\Phi = \Phi_1 \circ \dots \circ \Phi_T$ is a contraction on $(\mathbb{R}^n, \|\cdot\|_2)$ with contraction factor $s := \prod_{t=1}^T \kappa_t \in (0, 1)$. Consequently, Φ a unique fixed point $x^* \in \mathbb{R}^n$ such that for every starting point $x \in \mathbb{R}^n$ the iterates $\Phi^{\circ k}(x)$ (the k -fold composition of Φ with itself) converge to x^* at rate $\|\Phi^{\circ k}(x) - x^*\|_2 \leq s^k\|x - x^*\|_2$.

Moreover, every singular value of $J_{x^*}\Phi \in \mathbb{R}^{n \times n}$ satisfies $s_i(J_{x^*}\Phi) \leq s < 1$.

Proof The composition is again a contraction with contraction factor $s = \prod_{t=1}^T \kappa_t\|x - y\|_2 = s\|x - y\|_2$. The singular-value bound follows from $\|J_{x^*}\Phi\|_{\text{op}} \leq s < 1$. \blacksquare

3.2 Contraction in the Block-Max Norm

As a PIFS and diffusion work on patches, we now look at the *block-max norm* $\|x\|_{\infty, M} := \max_k \|x^{(k)}\|_2$, where $x^{(k)} \in \mathbb{R}^{n_k}$ denotes the vector of pixel values in patch R_k .

From (7), the Jacobian of Φ_t inherits the block structure directly from the score network.

Theorem 9 (Block-Max Contraction) Let $\hat{\varepsilon}_\theta(\cdot, t) : \mathbb{R}^n \rightarrow \mathbb{R}^n$ be C^1 . Denote by $[J_x\hat{\varepsilon}_\theta]_{kj} \in \mathbb{R}^{n_k \times n_j}$ the (k, j) block of the Jacobian. From (7), the corresponding blocks of $J_x\Phi_t$ are

$$[J_x\Phi_t]_{kk} = \frac{\sqrt{\bar{\alpha}_t - 1}}{\sqrt{\bar{\alpha}_t}} I_{n_k} + b_t [J_x\hat{\varepsilon}_\theta]_{kk} \in \mathbb{R}^{n_k \times n_k}, \quad [J_x\Phi_t]_{kj} = b_t [J_x\hat{\varepsilon}_\theta]_{kj} \in \mathbb{R}^{n_k \times n_j}, \quad k \neq j. \quad (15)$$

Define the score-coupling field $\mathcal{C}_{k,t} : \mathbb{R}^n \rightarrow \mathbb{R}_{\geq 0}$ by

$$\mathcal{C}_{k,t}(x) := |b_t| \sum_{j \neq k} \|[J_x\hat{\varepsilon}_\theta]_{kj}\|_{\text{op}} = \sum_{j \neq k} \|[J_x\Phi_t]_{kj}\|_{\text{op}}. \quad (16)$$

$\Phi_t : \mathbb{R}^n \rightarrow \mathbb{R}^n$ is a contraction in $(\mathbb{R}^n, \|\cdot\|_{\infty, M})$ if

$$\|[J_x\Phi_t]_{kk}\|_{\text{op}} + \mathcal{C}_{k,t}(x) < 1 \quad \text{holds for every patch } k \text{ and all } x \in \mathbb{R}^n. \quad (17)$$

Setting

$$\kappa_t^{\text{diag}} := \max_{1 \leq k \leq M} \sup_{x \in \mathbb{R}^n} \|[J_x \Phi_t]_{kk}\|_{\text{op}}, \quad \delta_t^{\text{cross}} := \max_{1 \leq k \leq M} \sup_{x \in \mathbb{R}^n} \mathcal{C}_{k,t}(x), \quad (18)$$

the contraction factor in $(\mathbb{R}^n, \|\cdot\|_{\infty, M})$ is

$$\kappa_t^{\text{pc}} := \kappa_t^{\text{diag}} + \delta_t^{\text{cross}} < 1. \quad (19)$$

Proof Fix $x, y \in \mathbb{R}^n$ and write $\delta_j := x^{(j)} - y^{(j)} \in \mathbb{R}^{n_j}$. Applying the fundamental theorem of calculus along the segment $z(\tau) := y + \tau(x - y)$ to the k -th patch output of the C^1 map Φ_t :

$$[\Phi_t(x)]^{(k)} - [\Phi_t(y)]^{(k)} = \int_0^1 \left([J_{z(\tau)} \Phi_t]_{kk} \delta_k + \sum_{j \neq k} [J_{z(\tau)} \Phi_t]_{kj} \delta_j \right) d\tau.$$

Taking $\|\cdot\|_2$ and using the triangle inequality:

$$\begin{aligned} \|[\Phi_t(x)]^{(k)} - [\Phi_t(y)]^{(k)}\|_2 &\leq \left(\|[J_z \Phi_t]_{kk}\|_{\text{op}} + \mathcal{C}_{k,t}(z) \right) \max_j \|\delta_j\|_2 \\ &\leq \kappa_t^{\text{pc}} \|x - y\|_{\infty, M}. \end{aligned}$$

■

Definition 10 ((PC): Block-Max Contraction) Φ_t satisfies (PC) whenever

$$\kappa_t^{\text{pc}} = \kappa_t^{\text{diag}} + \delta_t^{\text{cross}} < 1,$$

with

$$\kappa_t^{\text{diag}} = \max_{1 \leq k \leq M} \sup_{x \in \mathbb{R}^n} \|[J_x \Phi_t]_{kk}\|_{\text{op}}, \quad \delta_t^{\text{cross}} = \max_{1 \leq k \leq M} \sup_{x \in \mathbb{R}^n} \mathcal{C}_{k,t}(x) = |b_t| \sum_{j \neq k} \|[J_x \hat{\varepsilon}_\theta]_{kj}\|_{\text{op}}.$$

Corollary 11 Suppose (PC) holds for every Φ_t ($t \in \{1, \dots, T\}$) with respective factors $\kappa_t^{\text{pc}} \in (0, 1)$. Then the composition $\Phi = \Phi_1 \circ \dots \circ \Phi_T$ is a contraction on $(\mathbb{R}^n, \|\cdot\|_{\infty, M})$ with contraction factor

$$s^{\text{loc}} := \prod_{t=1}^T \kappa_t^{\text{pc}} \in (0, 1),$$

and therefore has a unique fixed point such that for every starting point $x \in \mathbb{R}^n$ the iterates $\Phi^{\circ k}(x)$ converge to x^* at rate $\|\Phi^{\circ k}(x) - x^*\|_{\infty, M} \leq (s^{\text{loc}})^k \|x - x^*\|_{\infty, M}$.

Proof Each Φ_t is a contraction on $(\mathbb{R}^n, \|\cdot\|_{\infty, M})$ with factor $\kappa_t^{\text{pc}} < 1$ by Theorem 9. The composition of finitely many contractions satisfies

$$\|\Phi(x) - \Phi(y)\|_{\infty, M} \leq \prod_{t=1}^T \kappa_t^{\text{pc}} \|x - y\|_{\infty, M} = s^{\text{loc}} \|x - y\|_{\infty, M}.$$

Since all norms on \mathbb{R}^n are equivalent, $(\mathbb{R}^n, \|\cdot\|_{\infty, M})$ is complete, and Theorem 4 gives the unique fixed point and convergence rate. ■

The theorem guarantees that repeatedly applying the PIFS Φ would eventually converge to a unique fixed point x^* . However in generative modelling we apply the composition Φ only once. We start from a noise vector x_T and produce an image x_0 by applying the composition $\Phi_1 \circ \dots \circ \Phi_T$. Different noise vectors generally map to different images under one application of Φ , but if we would iterate Φ all inputs would eventually lead to the same output.

The contraction in block-max norm guarantees stability and robustness: small perturbations in the input noise lead to controlled changes in the output’s coarse structure. The interplay between diagonal contractivity (κ_t^{diag}) and cross-patch coupling (δ_t^{cross}) in (PC) will show to be the lever through which the network can generate varied, realistic detail while maintaining global coherence.

3.3 Learning the Geometry: Training as Collage Minimisation

Properties (EC) and (PC) are geometric conditions on the operator Φ . We will show that the training objective actually drives the network toward satisfying them. Score-matching turns out to be, in Barnsley’s sense, the exact analogue of minimising collage error.

3.3.1 THE TRAINING OBJECTIVE AS COLLAGE ERROR

Theorem 12 (Collage analogue for Denoising Training) *The denoising objective*

$$\mathcal{L}(\theta) = \mathbb{E}_{t,x_0,\varepsilon}[\|\hat{\varepsilon}_\theta(x_t, t) - \varepsilon\|_2^2]$$

equals, up to timestep reweighting,

$$\sum_t \text{SNR}_t \mathbb{E}_{x_0,x_t}[\|\hat{x}_0(x_t, t) - x_0\|_2^2] \quad \text{with } \text{SNR}_t = \frac{\bar{\alpha}_t}{1 - \bar{\alpha}_t}. \quad (20)$$

Proof From the forward process (1) and the reparameterisation $\hat{x}_0 = (x_t - \sqrt{1 - \bar{\alpha}_t} \hat{\varepsilon}_\theta) / \sqrt{\bar{\alpha}_t}$, one obtains $\hat{\varepsilon}_\theta(x_t, t) - \varepsilon = \frac{\sqrt{\bar{\alpha}_t}}{\sqrt{1 - \bar{\alpha}_t}}(\hat{x}_0 - x_0)$, so $\|\hat{\varepsilon}_\theta(x_t, t) - \varepsilon\|_2^2 = \text{SNR}_t \|\hat{x}_0 - x_0\|_2^2$. Substituting gives (20), matching (B.5) of Ho et al. (2020). \blacksquare

The following theorem makes the quantitative link between score-matching and convergence to the fixed point precise.

3.3.2 COLLAGE-CONTRACTION BRIDGES

Theorem 13 (Collage-Contraction Bridge) *Under the assumptions of Corollary 11, let x^* be the unique fixed point of $\Phi = \Phi_1 \circ \dots \circ \Phi_T : \mathbb{R}^n \rightarrow \mathbb{R}^n$. Let $d_t := \|\Phi_t(x_t) - x_t\|_2$ be the one-step displacement at time t and set $c_t := \prod_{k=1}^{t-1} \kappa_k^{\text{pc}}$ (with $c_1 := 1$). Then:*

$$\|x^* - x_T\|_2 \leq \frac{1}{1 - s^{\text{loc}}} \sum_{t=1}^T c_t d_t. \quad (21)$$

Proof By Theorem 4 applied to Φ , $\|x_T - x^*\|_2 \leq \frac{1}{1 - s^{\text{loc}}} \|\Phi(x_T) - x_T\|_2$. Then

$$\Phi(x_T) - x_T = \sum_{t=1}^T [(\Phi_1 \circ \dots \circ \Phi_t)(x_T) - (\Phi_1 \circ \dots \circ \Phi_{t-1})(x_T)].$$

The t -th term equals $(\Phi_1 \circ \dots \circ \Phi_{t-1})(\Phi_t(x_t)) - (\Phi_1 \circ \dots \circ \Phi_{t-1})(x_t)$. Applying the Lipschitz bound of $\Phi_1 \circ \dots \circ \Phi_{t-1}$ (with factor c_t) gives $\|t\text{-th term}\|_2 \leq c_t d_t$. Summing over t and multiplying by $1/(1 - s^{\text{loc}})$ yields (21). \blacksquare

While Theorem 13 bounds the deterministic displacement of an individual sample path, generative modelling ultimately requires guarantees about probability measures. The following theorem lifts this trajectory-level bound to a distributional guarantee.

Concretely, the theorem bounds $\mathcal{W}_1(q(x_T), \delta_{x^*})$, the Wasserstein-1 distance from the *prior* $q(x_T)$ (the distribution of the initial noise) to the Dirac mass at the fixed point x^* . This is the statistical analogue of Barnsley’s Collage Theorem: minimising the score-matching objective during training not only pulls individual trajectories toward the fixed point but mathematically ensures the output measure aligns with δ_{x^*} . A small \mathcal{W}_1 distance guarantees that the generated distribution inherits the fractal geometry of the PIFS fixed point x^* , which in turn approximates the intrinsic dimension of the true data manifold.

Theorem 14 (L^2 - \mathcal{W}_1 Collage Bridge) *Let*

$$\mathcal{L}_t(\theta) = \mathbb{E}_{x_t} \|\hat{\varepsilon}_\theta(x_t, t) - \varepsilon_\theta^*(x_t, t)\|_2^2$$

be the excess score-matching risk at step t . Define the coupling weights $B_t := |b_t|$. Then

$$\mathcal{W}_1(q(x_T), \delta_{x^*}) \leq \frac{\sqrt{T}}{1 - s^{\text{loc}}} \left(\sum_{t=1}^T \left(\prod_{k < t} \kappa_k^{\text{pc}} \right)^2 \left(\sqrt{\mathbb{E}[\|\mathcal{R}_t\|_2^2]} + B_t \sqrt{\mathcal{L}_t(\theta)} \right)^2 \right)^{1/2}, \quad (22)$$

where δ_{x^} denotes the Dirac measure concentrated at the fixed point x^* , and $\mathcal{R}_t(x_t) := (\sqrt{\bar{\alpha}_{t-1}/\bar{\alpha}_t} - 1)x_t + b_t \varepsilon_\theta^*(x_t, t)$ is the schedule-geometry displacement under the true score (independent of θ).*

Proof $\mathcal{W}_1(\mu, \delta_{x^*}) = \mathbb{E}_{x_T \sim \mu} \|x_T - x^*\|_2$. Apply Theorem 13 and take expectations; Cauchy-Schwarz over t gives

$$\mathbb{E} \|x^* - x_T\|_2 \leq \frac{\sqrt{T}}{1 - s^{\text{loc}}} \left(\sum_t c_t^2 \mathbb{E}[d_t^2] \right)^{1/2}, \quad c_t = \prod_{k < t} \kappa_k^{\text{pc}}.$$

Here c_t is the Lipschitz factor of $\Phi_1 \circ \dots \circ \Phi_{t-1}$, the composition of all steps applied *after* step t in the reverse chain (steps with smaller index are applied last). In particular $c_1 = 1$ (empty product), corresponding to the final applied step Φ_1 , which receives the largest weight; early high-noise steps Φ_T carry weight $c_T \approx s^{\text{loc}} < 1$. Decompose the one-step displacement using (4):

$$\Phi_t(x_t) - x_t = \underbrace{\left(\frac{\sqrt{\bar{\alpha}_{t-1}}}{\sqrt{\bar{\alpha}_t}} - 1 \right) x_t + b_t \varepsilon_\theta^*(x_t, t)}_{=: \mathcal{R}_t(x_t)} + b_t (\hat{\varepsilon}_\theta(x_t, t) - \varepsilon_\theta^*(x_t, t)).$$

The second term is the score approximation error $b_t \xi_t$ where $\xi_t := \hat{\varepsilon}_\theta(x_t, t) - \varepsilon_\theta^*(x_t, t)$. \mathcal{R}_t depends only on x_t and the true score, so it is θ -free. Taking squared norms:

$$d_t^2 = \|\mathcal{R}_t\|_2^2 + 2b_t \langle \mathcal{R}_t, \xi_t \rangle + b_t^2 \|\xi_t\|_2^2.$$

For general θ , the cross-term satisfies by Cauchy-Schwarz:

$$|\mathbb{E}[\langle \mathcal{R}_t, \xi_t \rangle]| \leq \sqrt{\mathbb{E}[\|\mathcal{R}_t\|_2^2]} \cdot \sqrt{\mathcal{L}_t(\theta)},$$

so

$$\mathbb{E}[d_t^2] \leq \mathbb{E}[\|\mathcal{R}_t\|_2^2] + 2B_t \sqrt{\mathbb{E}[\|\mathcal{R}_t\|_2^2]} \sqrt{\mathcal{L}_t(\theta)} + B_t^2 \mathcal{L}_t(\theta) = \left(\sqrt{\mathbb{E}[\|\mathcal{R}_t\|_2^2]} + B_t \sqrt{\mathcal{L}_t(\theta)} \right)^2.$$

Substituting $\mathbb{E}[d_t^2]^{1/2} \leq \sqrt{\mathbb{E}[\|\mathcal{R}_t\|_2^2]} + B_t \sqrt{\mathcal{L}_t(\theta)}$ into the Cauchy-Schwarz bound gives (22). ■

Since the excess risk $\mathcal{L}_t(\theta) = \mathbb{E}\|\hat{\varepsilon}_\theta - \varepsilon_\theta^*\|_2^2$ is proportional to the reconstruction loss against the *conditional mean* $\mathbb{E}[x_0 | x_t]$: $\hat{\varepsilon}_\theta - \varepsilon_\theta^* = (\sqrt{\bar{\alpha}_t}/\sqrt{v_t})(\hat{x}_0 - \mathbb{E}[x_0 | x_t])$, giving $\mathcal{L}_t(\theta) = (\bar{\alpha}_t/v_t)\mathbb{E}\|\hat{x}_0 - \mathbb{E}[x_0 | x_t]\|_2^2$, the bound (22) holds equally in terms of the reconstruction objective, up to the substitution $B_t \rightarrow |b_t|\sqrt{\bar{\alpha}_t/v_t}$ inside the inner square root.

3.3.3 PIFS COLLAGE REGULARISER AND ENFORCEMENT OF (PC)

Theorem 15 (PIFS Collage Regulariser) *Define the PIFS collage loss $\mathcal{L}_{\text{PIFS}}(\theta) := \mathcal{L}(\theta) + \mu_{\text{reg}} \sum_{t,k,j \neq k} \|[J_x \hat{\varepsilon}_\theta]_{kj}\|_F^2$. Then:*

- (a) $\mathcal{L}_{\text{PIFS}}(\theta) = 0$ if and only if the score is perfect and all off-diagonal blocks vanish.
- (b) The gradient is computable in $O(M^2 n_k)$ JVP/VJP operations without materialising the full Jacobian.
- (c) Minimising $\mathcal{L}_{\text{PIFS}}$ strictly decreases a Cauchy-Schwarz upper bound on $\mathcal{C}_{k,t}(x)$, directly widening the (PC) contraction margin $1 - \kappa_t^{\text{diag}} - \delta_t^{\text{cross}}$.

Proof (a) Both terms are non-negative. (b) Each $[J]_{kj}v$ (JVP) and $u^\top [J]_{kj}$ (VJP) costs one forward pass; $O(n_k)$ per block gives $O(M^2 n_k)$ total. (c). Since $[J_x \Phi_t]_{kj} = b_t [J_x \hat{\varepsilon}_\theta]_{kj}$, any decrease in $\sum_{j \neq k} \|[J]_{kj}\|_F^2$ directly decreases the Cauchy-Schwarz upper bound

$$\mathcal{C}_{k,t}(x) = |b_t| \sum_{j \neq k} \|[J_x \hat{\varepsilon}_\theta]_{kj}\|_{\text{op}} \leq |b_t| \left(\sum_{j \neq k} \|[J]_{kj}\|_F^2 \right)^{1/2} \sqrt{M},$$

reducing $\delta_t^{\text{cross}} = \max_k \sup_x \mathcal{C}_{k,t}(x)$ and widening the margin in condition (17). ■

4 Two-Regime Structure of the Denoising Chain

The preceding section established *what* the geometric conditions are (Properties (EC) and (PC)) and *how* training enforces them through collage minimisation. The remaining question is *when* and *why* these conditions hold across the denoising chain. This requires computing κ_t^{diag} and δ_t^{cross} from actual data statistics and architectural properties.

4.1 Regime I: Global Context Assembly

Note that at high noise (t near T , $\bar{\alpha}_t \approx 0$), the cross-patch coupling $\delta_t^{\text{cross}} = O(\bar{\alpha}_t)$ is automatically negligible. We now study what happens in the next steps.

Theorem 16 (High-Noise Regime Contraction) *Suppose $\|x_0\|_2 \leq M$ almost surely, and assume the score network equals the true score: $\hat{\varepsilon}_\theta(x_t, t) = \varepsilon_\theta^*(x_t, t) = -\sqrt{v_t} \nabla_{x_t} \log p_t(x_t)$. Define*

$$\nu_t^* := \frac{1}{\sqrt{v_t}}, \quad \delta_t^* := \frac{CM^2\bar{\alpha}_t}{v_t^{3/2}}, \quad (23)$$

where $C > 0$ is an absolute constant depending only on the data distribution. Then $\delta_t^* = O(\bar{\alpha}_t)$ as $t \rightarrow T$, and (EC) holds at timestep t with $\nu_t^{\min} := \nu_t^*$ and $\delta_t := \delta_t^*$. Consequently, Φ_t is an Euclidean contraction with $\nu_t^* - \delta_t^* > L_t^*$, at all sufficiently high-noise steps under standard schedules.

Proof Since $\varepsilon_\theta^* = -\sqrt{v_t} \nabla_{x_t} \log p_t$,

$$J_{x_t} \varepsilon_\theta^* = -\sqrt{v_t} \nabla_{x_t}^2 \log p_t(x_t).$$

Applying Stein's identity to the Gaussian-mixture marginal

$$p_t(x_t) = \int \mathcal{N}(x_t; \sqrt{\bar{\alpha}_t}x_0, v_t I) p(x_0) dx_0$$

yields the decomposition of the log-density Hessian:

$$\nabla_{x_t}^2 \log p_t = \underbrace{-(1/v_t)I}_{\text{Gaussian term}} + \underbrace{(\bar{\alpha}_t/v_t^2) \text{Cov}(x_0 | x_t)}_{\text{posterior covariance}} + H_t(x_t),$$

where $H_t(x_t)$ collects all conditional cumulants of $x_0 | x_t$ beyond second order (so $H_t \equiv 0$ when $p(x_0 | x_t)$ is Gaussian). Multiplying through by $-\sqrt{v_t}$:

$$J_{x_t} \varepsilon_\theta^* = \frac{1}{\sqrt{v_t}} I - \frac{\bar{\alpha}_t}{v_t^{3/2}} \text{Cov}(x_0 | x_t) + E_t(x_t), \quad (24)$$

with $E_t(x_t) := -\sqrt{v_t} H_t(x_t)$. This is decomposition (9) with $\nu_t(x_t) := 1/\sqrt{v_t}$ and $R_t(x_t) := -(\bar{\alpha}_t/v_t^{3/2}) \text{Cov}(x_0 | x_t) + E_t(x_t)$.

Let us now bound $\|R_t\|_{\text{op}}$. Since $\|x_0\|_2 \leq M$, we have $\|\text{Cov}(x_0 | x_t)\|_{\text{op}} \leq M^2$, so $\|(\bar{\alpha}_t/v_t^{3/2}) \text{Cov}(x_0 | x_t)\|_{\text{op}} \leq M^2 \bar{\alpha}_t/v_t^{3/2}$. H_t is the tensor of conditional cumulants of order three and higher. The leading (third-order) term satisfies

$$\|H_t^{(3)}(x_t)\|_{\text{op}} \leq C_0 (\bar{\alpha}_t/v_t^2) \sup_{x_t} \mathbb{E}[\|x_0 - \mu_t\|_2^3 | x_t]$$

for an absolute constant $C_0 > 0$, where $\mu_t = \mathbb{E}[x_0 | x_t]$. Since $\|x_0\|_2 \leq M$ and $\|\mu_t\|_2 \leq M$, the bounded-support bound $\|x_0 - \mu_t\|_2 \leq 2M$ gives $\mathbb{E}[\|x_0 - \mu_t\|_2^3 | x_t] \leq 8M^3$, hence

$$\|E_t(x_t)\|_{\text{op}} \leq \frac{8C_0 M^3 \bar{\alpha}_t}{v_t^{3/2}} = O(\bar{\alpha}_t) \quad \text{as } t \rightarrow T. \quad (25)$$

Combining leads to $\delta_t^* := \|R_t\|_{\text{op}} \leq CM^2 \bar{\alpha}_t / v_t^{3/2}$ for a suitable absolute constant C absorbing both terms.

Both correction terms vanish as $O(\bar{\alpha}_t)$, so $\delta_t^* \rightarrow 0$. Meanwhile $\nu_t^* = 1/\sqrt{v_t} \rightarrow 1$, and the contraction margin $\nu_t^* - \delta_t^* - L_t^*$ is eventually positive under standard schedules. \blacksquare

Thus (EC) holds at high noise for any data distribution with bounded support, regardless of distributional shape.

Theorem 17 (Diagonal Block Expansion in the Fine-Detail Regime) *Let $p_{\text{data}} = \mathcal{N}(0, \Sigma_0)$ with Σ_0 block-diagonal with respect to the patch partition, $\Sigma_0 = \text{diag}(\Sigma_1, \dots, \Sigma_M)$, so that the patches $x_0^{(1)}, \dots, x_0^{(M)}$ are independent. Assume $\hat{\varepsilon}_\theta$ equals the true score ε_θ^* . For each patch $R_k \in \{1, \dots, M\}$, let*

$$\lambda_k := \|\Sigma_k\|_{\text{op}}$$

be the largest eigenvalue of the patch covariance and let $v_t = 1 - \bar{\alpha}_t$. Define the per-step diagonal expansion function $f_t : (0, \infty) \rightarrow \mathbb{R}$ by

$$f_t(\lambda) := \sqrt{\frac{\bar{\alpha}_t - 1}{\bar{\alpha}_t}} - |b_t| \frac{\sqrt{v_t}}{\lambda \bar{\alpha}_t + v_t}, \quad (26)$$

and the per-step patch expansion threshold

$$\lambda^*(t) := \frac{\sqrt{v_t}(\sqrt{v_t} - \sqrt{v_{t-1}})}{(\sqrt{\bar{\alpha}_{t-1}} - \sqrt{\bar{\alpha}_t})\sqrt{\bar{\alpha}_t}}. \quad (27)$$

Then the diagonal block spectral norm satisfies $\|[J_x \Phi_t]_{kk}\|_{\text{op}} = f_t(\lambda_k)$ for all $x \in \mathbb{R}^n$, with

- (a) $f_t(\lambda_k) < 1 \iff \lambda_k < \lambda^*(t)$;
- (b) $\lambda^*(t) > 1$ for any strictly decreasing schedule, so unit-variance patches ($\lambda_k = 1$) are always diagonally contractive;
- (c) $f_t(\lambda)$ is strictly increasing in λ .

Proof Under the block-diagonal Gaussian assumption with perfect score, the marginal score decomposes patch-wise. Differentiating the conditional mean $\hat{x}_0^{(k)}(x_t, t) = \Sigma_k(\Sigma_k + (v_t/\bar{\alpha}_t)I_{n_k})^{-1}x_t^{(k)}/\sqrt{\bar{\alpha}_t}$ and substituting into (7) gives, for any x :

$$[J_x \varepsilon_\theta^*]_{kk} = \frac{1}{\sqrt{v_t}}I_{n_k} - \frac{\sqrt{\bar{\alpha}_t}}{v_t}\Sigma_k \left(\Sigma_k + \frac{v_t}{\bar{\alpha}_t}I_{n_k} \right)^{-1}.$$

Combined with (4) and $b_t < 0$, the eigenvalue of $[J_x \Phi_t]_{kk}$ along an eigenvector of Σ_k with eigenvalue λ is precisely $f_t(\lambda)$ as in (26). Since $\partial f_t / \partial \lambda = |b_t| \sqrt{v_t} \bar{\alpha}_t / (\lambda \bar{\alpha}_t + v_t)^2 > 0$, f_t is strictly increasing (part (c)), and $\|[J_x \Phi_t]_{kk}\|_{\text{op}} = \max_i f_t(\mu_{k,i}) = f_t(\lambda_k)$, where $\mu_{k,i}$ are the eigenvalues of Σ_k .

At $\lambda = 1$, using $\bar{\alpha}_t + v_t = 1$ and $\bar{\alpha}_{t-1} + v_{t-1} = 1$,

$$f_t(1) = \sqrt{\bar{\alpha}_{t-1}\bar{\alpha}_t} + \sqrt{v_{t-1}v_t}.$$

As $\sqrt{\bar{\alpha}_{t-1}\bar{\alpha}_t} \leq (\bar{\alpha}_{t-1} + \bar{\alpha}_t)/2$ and $\sqrt{v_{t-1}v_t} \leq (v_{t-1} + v_t)/2$, we have that $f_t(1) \leq (\bar{\alpha}_{t-1} + \bar{\alpha}_t + v_{t-1} + v_t)/2 = 1$, with strict inequality when $\bar{\alpha}_{t-1} \neq \bar{\alpha}_t$. Thus $f_t(1) < 1$ and $\lambda^*(t) > 1$ (part (b)).

Setting $f_t(\lambda^*) = 1$ and solving for λ^* yields (27). Parts (a) then follows from strict monotonicity of f_t . \blacksquare

Hence under Gaussian data and the perfect score, the diagonal block of Φ_t contracts whenever $\lambda_k < \lambda^*(t)$.

4.1.1 DEVIATION OF THE TRAINED SCORE FROM THE GAUSSIAN SCORE

For non-Gaussian data the trained score deviates from the Gaussian score. Let $\varepsilon_\theta^\mathcal{N}(x_t, t)$ denote the score of the Gaussian surrogate $\mathcal{N}(0, \Sigma_0)$ and $\hat{\varepsilon}_\theta(x_t, t)$ the trained score. Define the *per-step deviation field*

$$\Delta_t(x) := \hat{\varepsilon}_\theta(x, t) - \varepsilon_\theta^\mathcal{N}(x, t), \quad (28)$$

and its Jacobian $\nabla_x \Delta_t(x)$. By linearity of the DDIM step (4) in the score, the diagonal block of the full Jacobian decomposes as

$$[J_x \Phi_t]_{kk} = [J_x \Phi_t^\mathcal{N}]_{kk} + b_t [\nabla_x \Delta_t(x)]_{kk}, \quad (29)$$

where $\Phi_t^\mathcal{N}$ is the DDIM step under the Gaussian score and $b_t < 0$.

Definition 18 (Directional Suppression and Suppression Margin) *Let Σ_k denote the empirical patch covariance of patch R_k over the training distribution, with top eigenvalue λ_k and top eigenvector $v_k^{(1)} \in \mathbb{R}^{n_k}$. For patch R_k at timestep t and $x \in \mathbb{R}^n$, define the directional suppression field along $v_k^{(1)}$*

$$S_{k,t}(x) := |b_t| \langle v_k^{(1)}, [\nabla_x \Delta_t(x)]_{kk} v_k^{(1)} \rangle, \quad (30)$$

and the suppression margin at (x, t)

$$\gamma_{k,t}(x) := S_{k,t}(x) - (f_t(\lambda_k) - 1). \quad (31)$$

Recall that the *Rayleigh quotient* of a matrix B along a unit vector v is $\langle v, Bv \rangle$, which equals the eigenvalue of B in direction v when v is an eigenvector.

Proposition 19 (Suppression Keeps Diagonal Rayleigh Quotient Below Unity) *Assume the patch covariance is isotropic, $\Sigma_k = \lambda_k I_{n_k}$. For patch R_k at timestep t and $x \in \mathbb{R}^n$, if $\gamma_{k,t}(x) > 0$ then $\langle v_k^{(1)}, [J_x \Phi_t]_{kk} v_k^{(1)} \rangle < 1$.*

Proof Under Gaussian p_{data} with $\Sigma_k = \lambda_k I_{n_k}$, $[J_x \Phi_t^\mathcal{N}]_{kk}$ is a scalar multiple of the identity with eigenvalue $f_t(\lambda_k)$ along every direction (Theorem 17). From (29) and $b_t < 0$, taking the Rayleigh quotient along $v_k^{(1)}$:

$$\langle v_k^{(1)}, [J_x \Phi_t]_{kk} v_k^{(1)} \rangle = f_t(\lambda_k) - |b_t| \langle v_k^{(1)}, [\nabla_x \Delta_t(x)]_{kk} v_k^{(1)} \rangle = f_t(\lambda_k) - S_{k,t}(x) < 1. \quad \blacksquare$$

The proposition identifies the precise condition under which a non-Gaussian trained score can maintain diagonal contractivity.

4.2 Regime II: Fine-Detail Synthesis

4.2.1 STRATIFIED CROSSOVER

All statements below are understood to hold $q(x_t)$ -almost surely; we write $\gamma_{k,t}$ for $\gamma_{k,t}(x_t)$ when the trajectory evaluation is clear from context.

Denote

$$\kappa_{k,t}^{\text{diag}} := \langle v_k^{(1)}, [J_x \Phi_t]_{kk} v_k^{(1)} \rangle = f_t(\lambda_k) - S_{k,t}(x). \quad (32)$$

Definition 20 (Per-patch release time) For patch R_k , we define the release time as

$$t_k^{\text{rel}} := \sup\{t \leq T : \gamma_{k,t}(x_t) \leq 0\}, \quad (33)$$

where $x_t \sim q(x_t)$.

Hence t_k^{rel} is the largest timestep, encountered while running the reverse chain from $t = T$, at which $\kappa_{k,t}^{\text{diag}}$ first reaches or exceeds 1.

Definition 21 ((MM): Margin Monotonicity) The score network $\hat{\epsilon}_\theta$ satisfies (MM) at timestep t if the following two conditions hold.

(MM1) **Spectral monotonicity.** The suppression margin $\gamma_{k,t}$ is strictly increasing in the patch variance λ_k :

$$\frac{\partial \gamma_{k,t}}{\partial \lambda_k} = \frac{\partial S_{k,t}}{\partial \lambda_k} - f'_t(\lambda_k) > 0. \quad (34)$$

By Theorem 17, $f'_t(\lambda_k) = |b_t| \sqrt{v_t} \bar{\alpha}_t / (\lambda_k \bar{\alpha}_t + v_t)^2 > 0$, so (34) requires $\partial S_{k,t} / \partial \lambda_k > f'_t(\lambda_k)$, so the learned suppression must grow with patch variance faster than the Gaussian baseline does.

(MM2) **Temporal decrease.** The margin is strictly decreasing along the reverse chain: $\partial_t \gamma_{k,t} < 0$ for every patch k . This guarantees that every patch eventually crosses from suppression ($\gamma_{k,t} > 0$) to release ($\gamma_{k,t} \leq 0$).

Theorem 22 (Stratified Crossover) Assume (MM).

- (a) **Release order.** If $\lambda_k < \lambda_{k'}$, then $t_k^{\text{rel}} > t_{k'}^{\text{rel}}$, so lower-variance patches release earlier in the reverse chain.
- (b) **Sign reversal of the Spearman rank.** For any two patches with $\lambda_k < \lambda_{k'}$ and any timestep $t \in [t_k^{\text{rel}}, t_{k'}^{\text{rel}})$:

$$\kappa_{k,t}^{\text{diag}} \geq 1 > \kappa_{k',t}^{\text{diag}},$$

so the pair (k, k') is discordant in the Spearman ranking of $(\lambda, \kappa_{\cdot,t}^{\text{diag}})$. Whether discordant pairs dominate globally, and hence $\rho(\lambda_k, \kappa_{k,t}^{\text{diag}}) < 0$, depends on the number of released patches at time t .

- (c) **Width of the stratified window.** To first order in λ_k , implicit differentiation of the release condition $\gamma_{k,t_k^{\text{rel}}} = 0$ gives

$$\frac{\partial t_k^{\text{rel}}}{\partial \lambda_k} = \frac{|\partial_\lambda \gamma_{k,t}|}{|\partial_t \gamma_{k,t}|} > 0, \quad (35)$$

and the total spread of release times across patches satisfies

$$\Delta t^{\text{strat}} \approx \frac{(\lambda_{\max} - \lambda_{\min}) \cdot |\partial_\lambda \gamma_{k,t}|}{|\partial_t \gamma_{k,t}|}, \quad (36)$$

evaluated at a representative variance $\bar{\lambda}$. Expanding via $\gamma_{k,t} = S_{k,t} - (f_t(\lambda_k) - 1)$:

$$\Delta t^{\text{strat}} \approx \frac{(\lambda_{\max} - \lambda_{\min}) \cdot (\partial_\lambda S_{k,t} - |b_t| \sqrt{v_t} \bar{\alpha}_t / (\bar{\lambda} \bar{\alpha}_t + v_t)^2)}{|\partial_t S_{k,t} - \partial_t f_t(\bar{\lambda})|}. \quad (37)$$

The derivatives $\partial_\lambda S_{k,t}$ and $\partial_t S_{k,t}$ depend on the trained network and can be estimated empirically.

- (d) **Restoration of the Gaussian ordering.** Once all patches have released, i.e. for $t < \min_k t_k^{\text{rel}}$, the Rayleigh quotient satisfies $\kappa_{k,t}^{\text{diag}} = f_t(\lambda_k) - S_{k,t} \geq 1$ for every k . As $S_{k,t} \rightarrow 0$ in deep Regime II, the ranking of $\kappa_{k,t}^{\text{diag}}$ across patches converges to that of $f_t(\lambda_k)$, which is strictly increasing in λ_k by Theorem 17(d), so $\rho(\lambda_k, \kappa_{k,t}^{\text{diag}})$ returns to positive values.

Proof (a) By (MM1), $\partial_{\lambda_k} \gamma_{k,t} > 0$, so lower-variance patches have strictly smaller margin. By (MM2), $\partial_t \gamma_{k,t} < 0$, so each margin decreases strictly over time and must eventually reach zero. The release condition $\gamma_{k,t_k^{\text{rel}}} = 0$ is therefore met at a strictly larger value of t for patches with smaller λ_k , giving $t_k^{\text{rel}} > t_{k'}^{\text{rel}}$ whenever $\lambda_k < \lambda_{k'}$.

(b) Fix $t \in [t_k^{\text{rel}}, t_{k'}^{\text{rel}})$. Since $t \geq t_k^{\text{rel}}$, patch R_k has released: $\gamma_{k,t} \leq 0$, equivalently $S_{k,t} \leq f_t(\lambda_k) - 1$, so $\kappa_{k,t}^{\text{diag}} = f_t(\lambda_k) - S_{k,t} \geq 1$. Since $t < t_{k'}^{\text{rel}}$, patch $R_{k'}$ remains suppressed: $\gamma_{k',t} > 0$, so $\kappa_{k',t}^{\text{diag}} < 1$ by Proposition 19. Hence $\kappa_{k,t}^{\text{diag}} \geq 1 > \kappa_{k',t}^{\text{diag}}$ despite $\lambda_k < \lambda_{k'}$, i.e. the pair is discordant.

- (c) Differentiate the identity $\gamma_{k,t_k^{\text{rel}}}(\lambda_k) = 0$ implicitly with respect to λ_k :

$$\partial_\lambda \gamma_{k,t} + \partial_t \gamma_{k,t} \cdot \frac{\partial t_k^{\text{rel}}}{\partial \lambda_k} = 0, \quad \text{so} \quad \frac{\partial t_k^{\text{rel}}}{\partial \lambda_k} = -\frac{\partial_\lambda \gamma_{k,t}}{\partial_t \gamma_{k,t}} = \frac{|\partial_\lambda \gamma_{k,t}|}{|\partial_t \gamma_{k,t}|} > 0,$$

where the positivity follows from (MM1) ($\partial_\lambda \gamma > 0$) and (MM2) ($\partial_t \gamma < 0$). Multiplying by $\lambda_{\max} - \lambda_{\min}$ and evaluating at representative $\bar{\lambda}$ yields (36). Substituting $\partial_\lambda \gamma = \partial_\lambda S_{k,t} - |b_t| \sqrt{v_t} \bar{\alpha}_t / (\bar{\lambda} \bar{\alpha}_t + v_t)^2$ and $\partial_t \gamma = \partial_t S_{k,t} - \partial_t f_t(\bar{\lambda})$ into (36) gives (37).

(d) For $t < \min_k t_k^{\text{rel}}$, all patches have released, so $\gamma_{k,t} \leq 0$ for every k . As suppression vanishes, $S_{k,t} \rightarrow 0$, and $\kappa_{k,t}^{\text{diag}} \rightarrow f_t(\lambda_k)$. Since $f_t(\lambda_k)$ is strictly increasing in λ_k by Theorem 17(d), the Spearman correlation $\rho(\lambda_k, \kappa_{k,t}^{\text{diag}})$ converges to positive values. \blacksquare

The theorem says that suppression is not released simultaneously across the image. Instead, low-variance patches cross the expansion threshold earlier in the reverse chain, while high-variance patches remain suppressed until later. This produces a moving window during which some patches are already expanding while others are still contracting, which is the source of the sign reversal in the Spearman rank correlation confirmed empirically in Section 7.5. Part (d) shows this inversion is transient: once all patches have released, the ranking reverts to the natural Gaussian order in which high-variance patches expand more strongly.

4.3 Training Origin of the Stratified Ordering

Theorem 22 derives the stratified release order as a consequence of (MM). We now give an heuristic argument that the training objective induces exactly the monotonicity required by (MM1).

Under a Gaussian patch model, the per-patch reconstruction loss at timestep t , defined as $\mathcal{L}_{k,t}(\theta) := \mathbb{E}[\|\hat{x}_0^{(k)} - x_0^{(k)}\|_2^2]$, evaluates to

$$\mathcal{L}_{k,t}(\theta) = \frac{\lambda_k v_t}{\bar{\alpha}_t \lambda_k + v_t}, \quad (38)$$

which is strictly increasing in the patch variance λ_k . High-variance patches therefore contribute more to the total loss at every noise level and at a training optimum the score network must allocate proportionally more correction to them.

To make this precise, we adopt three assumptions that are plausible for natural images, but cannot be established in full generality:

- (A1) the patch statistics are approximately Gaussian;
- (A2) per-patch losses are approximately equalised at convergence;
- (A3) the directional suppression satisfies $S_{k,t} \approx c_t \mathcal{L}_{k,t}(\theta)$ for some $c_t > 0$ independent of k .

Under (A1)–(A3), the derivative of $S_{k,t}$ with respect to λ_k is

$$\frac{\partial S_{k,t}}{\partial \lambda_k} \approx c_t \frac{\partial \mathcal{L}_{k,t}}{\partial \lambda_k} = \frac{c_t v_t^2}{(\bar{\alpha}_t \lambda_k + v_t)^2}.$$

The corresponding derivative of the Gaussian baseline is

$$f'_t(\lambda_k) = \frac{|b_t| \sqrt{v_t} \bar{\alpha}_t}{(\bar{\alpha}_t \lambda_k + v_t)^2}.$$

Both share the same denominator, so condition (MM1), namely $\partial_\lambda S_{k,t} > f'_t(\lambda_k)$, reduces to

$$c_t v_t^2 > |b_t| \sqrt{v_t} \bar{\alpha}_t, \quad (39)$$

which holds whenever c_t is sufficiently large or, for fixed c_t , at noise levels where v_t is large relative to $\bar{\alpha}_t$. Under (39) the suppression margin $\gamma_{k,t}$ is strictly increasing in λ_k , which is precisely (MM1). High-variance patches therefore release later in the reverse chain, producing the ordering of Theorem 22(a).

The underlying logic mirrors a principle from classical fractal image compression, where high-variance range blocks require more sustained encoder effort before their detail can be faithfully represented. Here the score network plays the analogous role: it sustains stronger suppression on high-variance patches and releases them progressively, enacting a learned prioritisation that concentrates reconstruction capacity where the per-patch loss is greatest.

4.4 Architectural Mechanism: Attention and the Two Regimes

The previous sections gave a complete account of κ_t^{diag} . In the high-noise limit of Regime I, (EC) holds and $\kappa_t^{\text{diag}} \approx 1/\sqrt{v_t} < 1$. Through Regime I, it is kept below 1 by the directional suppression field $S_{k,t}$ even though the Gaussian baseline $f_t(\lambda_k)$ would predict expansion. In Regime II suppression is released patch by patch in variance order, and $\kappa_{k,t}^{\text{diag}}$ climbs above 1 for each patch at its release time t_k^{rel} .

The remaining constant in (PC) is $\delta_t^{\text{cross}} = \max_k \sup_x \mathcal{C}_{k,t}(x)$, which is controlled by the architectural routing mechanism of the score network. We will bound it in terms of the score network’s attention weights.

Theorem 23 (Attention Block Structure of $J_x \Phi_t$) *Let $p = (p_1, \dots, p_M) \in \mathbb{R}^n$ denote the concatenated patch tokens with $p_k \in \mathbb{R}^{n_k}$, and consider a score network of the form $\hat{\epsilon}_\theta(p, t) = \text{FF}(A(p)W_V p) : \mathbb{R}^n \rightarrow \mathbb{R}^n$ without residual connections, where:*

- $d \in \mathbb{N}$ is the attention head dimension;
- $W_Q, W_K \in \mathbb{R}^{d \times n_k}$ are the query and key projection matrices;
- $W_V \in \mathbb{R}^{n_k \times n_k}$ is the value projection (applied per patch);
- $A(p) \in \mathbb{R}^{M \times M}$ is the attention weight matrix with (k, j) entry

$$A_{kj}(p) = \text{softmax}_j((W_Q p_k)^\top (W_K p_j) / \sqrt{d}),$$

where $\text{softmax}_j(z_j) := e^{z_j} / \sum_\ell e^{z_\ell}$ normalises across the j -index so that $\sum_j A_{kj}(p) = 1$ for each k ;

- $\text{FF} : \mathbb{R}^n \rightarrow \mathbb{R}^n$ is a feedforward network with per-patch Lipschitz constants $L_{\text{ff},k}$, meaning $\|[J_{p'} \text{FF}]_{kk}\|_{\text{op}} \leq L_{\text{ff},k}$.

Then:

- (a) *The cross-patch Jacobian blocks satisfy*

$$\|[J_x \hat{\epsilon}_\theta]_{k\ell}\|_{\text{op}} \leq L_{\text{ff},k} (A_{k\ell} \|W_V\|_{\text{op}} + \|p\|_2 \|\nabla_x A_{k\ell}\|_{\text{op}} \|W_V\|_{\text{op}}).$$

- (b) *The cross-patch coupling field satisfies*

$$\delta_t^{\text{cross}} \leq |b_t| L_{\text{ff}} (1 + \|p\|_2 \max_{k,\ell} \|\nabla_x A_{k\ell}\|_{\text{op}}) \|W_V\|_{\text{op}} \max_k \sum_{j \neq k} A_{kj}(x), \quad (40)$$

where $L_{\text{ff}} := \max_k L_{\text{ff},k}$.

- (c) *The diagonal blocks satisfy $\|[J_x \hat{\epsilon}_\theta]_{kk}\|_{\text{op}} \leq L_{\text{ff},k}(A_{kk}\|W_V\|_{\text{op}} + \|p_k\|_2 \|\nabla_x A_{kk}\|_{\text{op}} \|W_V\|_{\text{op}})$.*
- (d) *In the hard-attention limit $\tau \rightarrow 0$, where $A_{kj} \rightarrow \mathbf{1}[j = j^*(k)]$ for a winner-take-all assignment $j^*(k)$, all cross-patch blocks with $j \neq j^*(k)$ vanish and $\delta_t^{\text{cross}} = 0$.*

Proof *Attention Jacobian.* For $p'_k = \sum_j A_{kj}(x)(W_V p_j)$, differentiating with respect to p_ℓ :

$$\frac{\partial p'_k}{\partial p_\ell} = A_{k\ell}(x)W_V + \sum_j \frac{\partial A_{kj}(x)}{\partial p_\ell}(W_V p_j). \quad (41)$$

The first term has norm $A_{k\ell}\|W_V\|_{\text{op}}$; the second is bounded by $\|W_V\|_{\text{op}}\|p\|_2\|\nabla_x A_{k\ell}\|_{\text{op}}$ by Cauchy-Schwarz..

Feedforward composition. Without residual connection,

$$[J_x \hat{\epsilon}_\theta]_{k\ell} = [J_{p'} \text{FF}]_{kk} \cdot (\partial p'_k / \partial p_\ell)$$

with $\|[J_{p'} \text{FF}]_{kk}\|_{\text{op}} \leq L_{\text{ff},k}$, giving parts (a) and (c).

(b) Sum over $\ell \neq k$ and multiply by $|b_\ell|$ to get (40), using $L_{\text{ff}} := \max_k L_{\text{ff},k}$ to pass to a single global Lipschitz constant. Note that $\sum_{j \neq k} A_{kj}(x) = 1 - A_{kk}(x) \leq 1$ since softmax weights sum to 1 and $A_{kk} \geq 0$, so $\max_k \sum_{j \neq k} A_{kj}(x) \leq 1$, confirming the bound is finite.

(d) As $\tau \rightarrow 0$: $A_{kj} \rightarrow \mathbf{1}[j = j^*(k)]$ and $\partial A_{kj} / \partial p_\ell \rightarrow 0$ for $j \neq j^*(k)$. \blacksquare

The bound in part (b) contains $\|\nabla_x A_{k\ell}\|_{\text{op}}$, the operator norm of the gradient of the softmax weight with respect to input tokens, which is dense and depends on the query/key matrices and the input. Its regime-dependent behaviour is well-characterised: near the hard-attention limit ($\tau \rightarrow 0$, equivalently Regime II), $A_{kj} \rightarrow \mathbf{1}[j = j^*(k)]$ is piecewise constant so $\nabla_x A_{k\ell} \rightarrow 0$ except at assignment boundaries, so the bound tightens to part (d). In Regime I, $\nabla_x A_{k\ell}$ is non-negligible, but appears only in δ_t^{cross} , which is already large empirically, so the bound is loose, but directionally correct. A sharper characterisation in terms of query/key temperature is left for future work.

Equation (40) connects the two-regime structure directly to attention locality and the constants of (PC). In the high-noise limit of Regime I, (EC) holds by the isotropic dominance mechanism of Theorem 16, independently of the block structure. The attention bound is consistent with this, as diffuse weights keep δ_t^{cross} small relative to the large isotropic contraction margin. The bound (40) shows that δ_t^{cross} is controlled by $\max_k \sum_{j \neq k} A_{kj}(x)$, the total off-diagonal attention weight. When attention is diffuse, this sum is close to $1 - 1/M$ and δ_t^{cross} is large. When attention localises toward the diagonal ($A_{kk} \rightarrow 1$), the off-diagonal sum tends to zero and, in the hard-attention limit of part (d), $\delta_t^{\text{cross}} = 0$. The Regime I/II transition is thus tied to whether attention is diffuse or local, a connection that the empirical measurements of Section 7.4 verify directly.

Theorem 23 is stated for a network without residual connections and models only the attention contribution to the Jacobian. Three components of real architectures shape δ_t^{cross} and play distinct roles.

1. **Self-attention** (Diffusion Transformers (Peebles and Xie, 2023)) is the *explicit* global routing mechanism. The mechanism

$$p'_k = \sum_j A_{kj}(W_V p_j), \quad A_{kj} = \text{softmax}\left(\frac{(W_Q p_k)^\top (W_K p_j)}{\sqrt{d}}\right), \quad (42)$$

implements a soft, differentiable analogue of the PIFS domain-range structure: query tokens $\{p_k\}$ are range blocks; key/value tokens are domain blocks; A_{kj} is the soft domain-range assignment; and $W_V p_j$ is the local map. In the hard-attention limit $\tau \rightarrow 0$, $A_{kj} \rightarrow \mathbf{1}[j = j^*(k)]$ and the classical PIFS structure is recovered exactly. Theorem 23 proves that δ_t^{cross} is bounded by the attention weights, and the two-regime structure follows from how broadly versus locally attention broadcasts at each noise level.

2. **Within-block residuals** (Diffusion Transformers (Peebles and Xie, 2023)): connections of the form $p_k \leftarrow p_k + p'_k$ add an identity term, $\partial(p_k + p'_k)/\partial p_\ell = \mathbf{1}[k = \ell]I + \partial p'_k/\partial p_\ell$. Diagonal blocks increase by at most a constant of 1; cross-patch blocks are unaffected since the identity residual contributes no off-diagonal term.
3. **Encoder skip connections** (UNet architectures (Ho et al., 2020)) contribute a *localised structural residual*: their Jacobians have non-zero cross-patch blocks determined by convolutional receptive fields and persist even as attention localises in Regime II. The bound (40) therefore covers only the attention component of δ_t^{cross} . The full cross-patch coupling satisfies $\delta_t^{\text{cross}} \leq \delta_t^{\text{cross,attn}} + \delta_t^{\text{cross,skip}}$, where $\delta_t^{\text{cross,skip}}$ is bounded by $|b_t| \|J^{\text{skip}}\|_{\text{cross}}$ with $\|J^{\text{skip}}\|_{\text{cross}}$ depending on the convolutional filter weights and receptive field rather than on the attention pattern. In Regime II, $\delta_t^{\text{cross,attn}}$ declines as attention localises, but $\delta_t^{\text{cross,skip}}$ remains a non-trivial lower bound on the total cross-patch coupling and may dominate at the finest spatial resolution. This is consistent with the empirical spike in δ_t^{cross} analysed in Section 7.4, where the decoder operates at finest resolution and the skip connection from the first encoder stage spans several patches.

5 Attractor Geometry

Sections 3 and 4 established Properties (EC) and (PC) and characterised the two-regime structure of the denoising chain. This section analyses the *fractal geometry* of the resulting PIFS attractor of Φ , in terms of size and how the chosen schedule controls it.

The central tool is the Kaplan-Yorke dimension (Kaplan and Yorke, 1979), which quantifies the fractal dimension of an attractor from the Lyapunov spectrum of the system at its fixed point. Under Gaussian data and the block-diagonal covariance structure of Theorem 17, the Lyapunov exponents at x^* can be computed in closed form as a function of patch variances and the noise schedule, yielding an explicit dimension formula. For non-Gaussian data, the directional suppression field $S_{k,t}(x)$ of Section 4.1.1 modifies this formula, and the two formulas together, Gaussian baseline into a suppression-corrected version.

5.1 Lyapunov Exponents and the Degenerate Baseline

For a classical IFS with contraction ratios $\{s_i\}_{i=1}^N$, the Hausdorff dimension of the attractor solves the Moran equation $\sum_i s_i^d = 1$ (Falconer, 1990). For a PIFS, the natural analogue is the Kaplan-Yorke dimension (Kaplan and Yorke, 1979), which is defined from the Lyapunov exponents of the operator at its fixed point.

Define the *Lyapunov exponents* at the fixed point x^* by¹

$$\ell_i := \frac{1}{T} \log s_i(J_{x^*} \Phi), \quad (43)$$

where $s_i(\cdot)$ denotes the i -th singular value in decreasing order, and $J_{x^*} \Phi = \prod_{t=1}^T J_{x_t^*} \Phi_t$ is the chain-rule product along the fixed point trajectory, with $x_T^* = x^*$ and $x_{t-1}^* = \Phi_t(x_t^*)$.

The *Kaplan-Yorke* (KY) dimension is given by

$$d_{\text{KY}}(\mathcal{A}) = j^* + \frac{\sum_{i=1}^{j^*} \ell_i}{|\ell_{j^*+1}|}, \quad j^* = \max\{j : \sum_{i=1}^j \ell_i \geq 0\}. \quad (44)$$

Proposition 24 (KY Dimension under Global Contraction) *Under (EC), all Lyapunov exponents satisfy $\ell_i \leq \frac{1}{T} \log s < 0$, so $j^* = 0$ and $d_{\text{KY}}(\mathcal{A}) = 0$.*

Proof Every singular value $s_i(J_{x^*} \Phi)$ is at most $s < 1$. ■

The degenerate baseline with global contractivity collapses the attractor dimension to zero. We now show that (PC), which requires patch-wise diagonal contractivity with bounded cross-patch coupling, is exactly the structure under which $d_{\text{KY}} > 0$ becomes possible.

5.2 The Expansion Threshold via the Discrete Moran Equation

Theorem 25 (The Discrete Moran Equation and Expansion Threshold)

Let $p_{\text{data}} = \mathcal{N}(0, \Sigma_0)$ with block-diagonal covariance $\Sigma_0 = \text{diag}(\Sigma_1, \dots, \Sigma_M)$ and let $\hat{\varepsilon}_\theta$ equal the true score ε_θ^* . For each patch R_k , let $\mu_{k,1} \geq \mu_{k,2} \geq \dots \geq \mu_{k,n_k} \geq 0$ be the eigenvalues of Σ_k in decreasing order, with $\mu_{k,1} = \lambda_k$. Define the mean Lyapunov exponent function $\Lambda : (0, \infty) \rightarrow \mathbb{R}$ by $\Lambda(\mu) := \frac{1}{T} \sum_{t=1}^T \log f_t(\mu)$, and the global expansion threshold $\lambda^{**} > 1$ as the unique solution to

$$\prod_{t=1}^T f_t(\lambda^{**}) = 1. \quad (45)$$

Then

- (a) For any $\mu > \lambda^{**}$, $\Lambda(\mu) > 0$.
- (b) Setting $M^{++} := \sum_{k=1}^M \#\{i : \mu_{k,i} > \lambda^{**}\}$, we have $d_{\text{KY}}(\mathcal{A}) \geq M^{++}$, and $d_{\text{KY}} > 0$ whenever any patch satisfies $\lambda_k > \lambda^{**}$.
- (c) $\lambda^{**} > \min_t \lambda^*(t)$.

1. Since x^* is a fixed point of Φ , we have $J_{x^*} \Phi^k = (J_{x^*} \Phi)^k$ for all $k \geq 1$.

Proof The function $G(\lambda) := \prod_{t=1}^T f_t(\lambda)$ is continuous and strictly increasing as each f_t is strictly increasing by Theorem 17(d). By Theorem 17(c), $G(1) < 1$. As $\lambda \rightarrow \infty$, $\lambda \bar{\alpha}_t \gg v_t$ at each step, so $f_t(\lambda) \rightarrow \sqrt{\bar{\alpha}_{t-1}/\bar{\alpha}_t}$ and $G(\lambda) \rightarrow \prod_t \sqrt{\bar{\alpha}_{t-1}/\bar{\alpha}_t} = \sqrt{\bar{\alpha}_0/\bar{\alpha}_T} = 1/\sqrt{\bar{\alpha}_T} > 1$. By the intermediate value theorem, a unique $\lambda^{**} > 1$ satisfies (45).

Under block-diagonal Σ_0 the patches are independent and by (1) so are the noised patches $x_t^{(k)}$. The marginal score decomposes as $\nabla_{x_t} \log p_t(x_t) = \sum_k \nabla_{x_t^{(k)}} \log p_t^{(k)}(x_t^{(k)})$, so $J_{x^*} \Phi$ is block-diagonal with the same patch partition. The eigenvalue of the k -th block along the i -th eigenvector of Σ_k is $\prod_{t=1}^T f_t(\mu_{k,i})$, giving Lyapunov exponent $\Lambda(\mu_{k,i})$.

(a) For $\mu > \lambda^{**}$, $G(\mu) > G(\lambda^{**}) = 1$, so $\Lambda(\mu) = \frac{1}{T} \log G(\mu) > 0$.

(b) Exactly M^{++} Lyapunov exponents are positive, so $j^* \geq M^{++}$ and $d_{\text{KY}} \geq M^{++} > 0$.

(c) Let $\lambda_0 = \min_t \lambda^*(t)$ with minimiser t^* . By definition $f_{t^*}(\lambda_0) = 1$. For all $t \neq t^*$, monotonicity and $\lambda_0 \leq \lambda^*(t)$ give $f_t(\lambda_0) \leq 1$, hence $G(\lambda_0) \leq 1$. Equality $G(\lambda_0) = 1$ would require $\lambda^*(t) = \lambda_0$ for every t , which forces v_t/v_{t-1} to be constant across all steps, i.e. a geometric progression in v_t . Any schedule whose ratio v_t/v_{t-1} is not identically constant gives $G(\lambda_0) < 1 = G(\lambda^{**})$ and hence $\lambda^{**} > \lambda_0$. \blacksquare

Continuous-time limit. For $T \rightarrow \infty$ with the noise schedule viewed as a continuous function $\bar{\alpha} : [0, 1] \rightarrow (0, 1]$, the discrete product $G(\lambda) = \prod_{t=1}^T f_t(\lambda)$ converges to the exponential of a Riemann sum: $G(\lambda) \rightarrow \exp(\int_0^1 \log f(\lambda, t) dt)$. The Moran equation $G(\lambda^{**}) = 1$ therefore becomes $\int_0^1 \log f(\lambda^{**}, t) dt = 0$ in the continuous-time limit, consistent with the probability flow ODE framework of Song et al. (2021b). In this limit the stratified crossover (Theorem 22) remains well-defined, with the release time t_k^{rel} converging to the zero of the continuous-time margin $\gamma_k(t) = S(t) - (f(\lambda_k, t) - 1)$.

5.3 The KY Dimension Formula: Gaussian and Non-Gaussian Data

Under the Gaussian baseline, the block-diagonal structure of $J_{x^*} \Phi$ allows the Lyapunov spectrum to be computed in closed form, yielding an explicit dimension formula. The following two theorems derive this formula and its extension to non-Gaussian data.

Theorem 26 (Exact KY Dimension Formula Under Gaussian Data) *Under the hypotheses of Theorem 25, assume additionally that all patch covariances are isotropic, with $\Sigma_k = \lambda_k I_{n_k}$ for each k . Under this assumption, all n_k Lyapunov exponents for patch R_k equal $\Lambda(\lambda_k)$, and the full Lyapunov spectrum is the multi-set $\{\Lambda(\lambda_k) \text{ repeated } n_k \text{ times}\}_{k=1}^M$. Set $N^+ := \sum_{k:\lambda_k > \lambda^{**}} n_k$ (total dimension of expanding directions) and let*

$$k^* := \arg \max_{k:\lambda_k < \lambda^{**}} \lambda_k$$

be the index of the contractive patch with the highest variance (so $\Lambda_{k^}^- := \Lambda(\lambda_{k^*}) < 0$ is the least-negative contracting exponent). Assume*

$$\sum_{k:\lambda_k > \lambda^{**}} n_k \Lambda(\lambda_k) < |\Lambda_{k^*}^-|, \quad (46)$$

which ensures that the KY cutoff index is exactly $j^* = N^+$. Then:

$$d_{\text{KY}}(\mathcal{A}) = N^+ + \frac{\sum_{k:\lambda_k > \lambda^{**}} n_k \Lambda(\lambda_k)}{|\Lambda_{k^*}^-|}. \quad (47)$$

Without condition (46), setting $\Lambda^+ := \min_{k:\lambda_k > \lambda^{**}} \Lambda(\lambda_k) > 0$, leads to the lower bound $d_{\text{KY}}(\mathcal{A}) \geq N^+ + N^+ \Lambda^+ / |\Lambda_{k^*}^-|$.

Proof All n_k eigenvalues of Σ_k equal λ_k , so all n_k Lyapunov exponents for patch R_k equal $\Lambda(\lambda_k)$. By Theorem 25(a), $\Lambda(\lambda_k) > 0$ for $\lambda_k > \lambda^{**}$ and $\Lambda(\lambda_k) < 0$ for $\lambda_k < \lambda^{**}$. Ordering the full Lyapunov spectrum in decreasing order: the first N^+ exponents are $\Lambda(\lambda_k) > 0$, and the $(N^+ + 1)$ -th is $\Lambda_{k^*}^- < 0$. Condition (46) is precisely the requirement that $\sum_{k:\lambda_k > \lambda^{**}} n_k \Lambda(\lambda_k) + \Lambda_{k^*}^- < 0$, i.e. that including the $(N^+ + 1)$ -th exponent turns the partial sum negative, so $j^* = N^+$ in the KY formula (44). Substituting gives (47). The lower bound $d_{\text{KY}} \geq N^+ + N^+ \Lambda^+ / |\Lambda_{k^*}^-|$ follows from $\Lambda(\lambda_k) \geq \Lambda^+ > 0$ for all k with $\lambda_k > \lambda^{**}$. Since the partial sum of the first N^+ exponents equals $\sum_{k:\lambda_k > \lambda^{**}} n_k \Lambda(\lambda_k) > 0$ by Theorem 25(a), the KY definition gives $j^* \geq N^+$. Using the lower bound $\Lambda(\lambda_k) \geq \Lambda^+$ in the numerator and the fact that $j^* \geq N^+$ then yields the stated bound, and holds regardless of whether condition (46) is satisfied. ■

The Gaussian formula of Theorem 26 applies when the score is exactly the Gaussian surrogate. For a trained network on real data, the score deviates from this surrogate through the suppression field $S_{k,t}$ of Section 4.1.1, modifying the diagonal eigenvalues and thereby the attractor dimension. The following theorem makes this precise.

Theorem 27 (Suppression-Corrected Kaplan-Yorke Dimension) *Adopt the hypotheses of Theorem 26 (isotropic patches $\Sigma_k = \lambda_k I_{n_k}$, and the perfect score assumption inherited from Theorem 25). For each patch R_k and timestep t , let*

$$S_{k,t}(x) = |b_t| \langle v_k^{(1)}, [\nabla_x \Delta_t(x)]_{kk} v_k^{(1)} \rangle > 0$$

denote the directional suppression field (Definition 18), evaluated at $x = x_t$ sampled from the forward marginal $q(x_t)$. As in Definition 20, all subsequent statements involving $S_{k,t}$ are understood to hold $q(x_t)$ -almost surely, and we write $S_{k,t}$ for $S_{k,t}(x_t)$ when the trajectory evaluation is clear from context. Define the suppression-corrected diagonal factor

$$g_{k,t} := f_t(\lambda_k) - S_{k,t}(x_t), \quad (48)$$

and the suppression-corrected Lyapunov exponent

$$\Lambda_{\text{eff},k} := \frac{1}{T} \sum_{t=1}^T \mathbb{E}_{x_t \sim q(x_t)} [\log g_{k,t}]. \quad (49)$$

Assume $S_{k,t} < f_t(\lambda_k)$ for all k, t (suppression does not reverse the sign of the diagonal factor), and that there exists at least one patch R_k with $\Lambda_{\text{eff},k} > 0$. Define the suppression-corrected expanding set $\mathcal{K}^{+++} := \{k : \Lambda_{\text{eff},k} > 0\}$, with $N^{+++} := \sum_{k \in \mathcal{K}^{+++}} n_k$, and let $k^{**} := \arg \max_{k \notin \mathcal{K}^{+++}} \lambda_k$ be the contractive patch closest to the expanding set. Then

- (a) For every patch R_k : $\Lambda_{\text{eff},k} \leq \Lambda(\lambda_k)$, with equality if and only if $S_{k,t} = 0$ for all t . Consequently $\mathcal{K}^{+++} \subseteq \mathcal{K}^+$ (the expanding set can only shrink) and $N^{+++} \leq N^+$. So suppression
- (b) The suppression-corrected Kaplan-Yorke dimension is

$$d_{\text{KY}}^{\text{eff}}(\mathcal{A}) = N^{+++} + \frac{\sum_{k \in \mathcal{K}^{+++}} n_k \Lambda_{\text{eff},k}}{|\Lambda_{\text{eff},k^{**}}|}, \quad (50)$$

under the condition that $\sum_{k \in \mathcal{K}^{+++}} n_k \Lambda_{\text{eff},k} < |\Lambda_{\text{eff},k^{**}}|$ (the analogue of condition (46)).

- (c) $d_{\text{KY}}^{\text{eff}}(\mathcal{A}) \leq d_{\text{KY}}(\mathcal{A})$, with equality if and only if $S_{k,t} = 0$ for all k, t .

Proof (a) Since $S_{k,t}(x_t) > 0$ almost surely, $g_{k,t} = f_t(\lambda_k) - S_{k,t}(x_t) \leq f_t(\lambda_k)$ almost surely, with equality iff $S_{k,t}(x_t) = 0$. By Jensen's inequality, $\Lambda_{\text{eff},k} = \frac{1}{T} \sum_t \mathbb{E}[\log g_{k,t}] \leq \frac{1}{T} \sum_t \log \mathbb{E}[g_{k,t}] \leq \frac{1}{T} \sum_t \log f_t(\lambda_k) = \Lambda(\lambda_k)$, where the second inequality uses $\mathbb{E}[g_{k,t}] \leq f_t(\lambda_k)$ (since $S_{k,t} \geq 0$). If $\Lambda_{\text{eff},k} > 0$ then $\Lambda(\lambda_k) \geq \Lambda_{\text{eff},k} > 0$, so $k \in \mathcal{K}^+$; thus $\mathcal{K}^{+++} \subseteq \mathcal{K}^+$.

(b) Under the perfect score assumption, $J_{x^*} \Phi$ is block-diagonal with per-patch eigenvalue $\prod_t g_{k,t}$ along the leading direction of patch R_k (replacing $f_t(\lambda_k)$ by $g_{k,t}$ throughout the proof of Theorem 26). The Lyapunov exponent for patch R_k is $\Lambda_{\text{eff},k}$, which is positive iff $k \in \mathcal{K}^{+++}$. Formula (50) then follows from the Kaplan-Yorke definition (44) with $j^* = N^{+++}$, using the stated analogue of condition (46).

(c) Let $\{\ell_i\}_{i=1}^n$ denote the Gaussian Lyapunov spectrum $\{\Lambda(\lambda_k)$ repeated n_k times} sorted in decreasing order, and $\{\ell'_i\}_{i=1}^n$ the suppressed spectrum $\{\Lambda_{\text{eff},k}$ repeated n_k times} likewise sorted. From part (a), $\Lambda_{\text{eff},k} \leq \Lambda(\lambda_k)$ for every k , so the unsorted suppressed values are componentwise dominated by the Gaussian values. By the rearrangement inequality, the same dominance holds after sorting: $\ell'_i \leq \ell_i$ for all i . Consequently $\sum_{i=1}^j \ell'_i \leq \sum_{i=1}^j \ell_i$ for every j , so $j^{**} \leq j^*$ where $j^{**} = \max\{j : \sum_{i \leq j} \ell'_i \geq 0\}$ and $j^* = \max\{j : \sum_{i \leq j} \ell_i \geq 0\}$.

Case A ($j^{**} < j^*$): $d_{\text{KY}}^{\text{eff}} = j^{**} + \text{frac} < j^{**} + 1 \leq j^* \leq d_{\text{KY}}$.

Case B ($j^{**} = j^*$): The numerator $\sum_{i \leq j^*} \ell'_i \leq \sum_{i \leq j^*} \ell_i$ (from the pointwise dominance), and the denominator $|\ell'_{j^*+1}| \geq |\ell_{j^*+1}|$ (since $\ell'_{j^*+1} \leq \ell_{j^*+1} < 0$). Hence the fractional part of $d_{\text{KY}}^{\text{eff}}$ is at most that of d_{KY} , giving $d_{\text{KY}}^{\text{eff}} \leq d_{\text{KY}}$.

In both cases equality holds iff all inequalities are equalities, i.e. iff $S_{k,t} = 0$ for all k, t . ■

The Gaussian formula of Theorem 26 is recovered exactly when $S_{k,t} = 0$ for all k, t . The release time t_k^{rel} governs *when* each patch begins to contribute to d_{KY} during the chain; whether a patch belongs to \mathcal{K}^{+++} and contributes to the *final* $d_{\text{KY}}^{\text{eff}}$ depends on the sign of $\Lambda_{\text{eff},k}$ integrated over all T steps (Theorem 27).

6 Practical Implications

The two-regime structure and the attractor geometry are each governed by constants that depend on the same noise schedule and patch covariance spectrum. Because L_t^* , $f_t(\lambda)$, and $S_{k,t}$ are all computable from the schedule and patch spectrum without running the model, they form a unified design language for schedule and loss choices.

6.1 L_t^* : Equalisation Impossibility and Asymptotic Scaling

The contraction threshold L_t^* of Theorem 6 depends only on the noise schedule, not on the data or the architecture. A natural question is whether the schedule can be chosen to equalise L_t^* across steps, making the contraction chain uniformly strong.

Theorem 28 (Impossibility of Strict L_t^* -Equalisation) *For any strictly decreasing schedule with $\bar{\alpha}_0 = 1$, no constant $L^* > 0$ satisfies $L_t^* = L^*$ for all $t \in \{1, \dots, T\}$, $T \geq 3$.*

Proof Suppose $L_t^* = L^*$ for all t . From (10), $\sqrt{\bar{\alpha}_{t-1}/\bar{\alpha}_t} - 1 = L^*|b_t| = L^*(\sqrt{\bar{\alpha}_{t-1}/\bar{\alpha}_t}\sqrt{v_t} - \sqrt{v_{t-1}})$. Rearranging gives $h(\bar{\alpha}_{t-1})/h(\bar{\alpha}_t) = \sqrt{\bar{\alpha}_{t-1}/\bar{\alpha}_t}$ where $h(a) := 1 - L^*\sqrt{1-a}$, which forces $h(\bar{\alpha}_t) = C\sqrt{\bar{\alpha}_t}$ for some constant C independent of t . Since $\bar{\alpha}_0 = 1$ (by convention), evaluating at $t = 0$ gives $h(1) = 1 - L^* \cdot 0 = 1 = C\sqrt{1}$, so $C = 1$ and hence $h(\bar{\alpha}_t) = \sqrt{\bar{\alpha}_t}$, i.e. $g(\bar{\alpha}_t) := L^*\sqrt{1-\bar{\alpha}_t} + \sqrt{\bar{\alpha}_t} = 1$ for all t . Since $g''(a) = -L^*/(4(1-a)^{3/2}) - 1/(4a^{3/2}) < 0$, g is strictly concave and $g(a) = 1$ has at most two solutions. For $T \geq 3$ this is a contradiction. ■

The practical relaxation is to minimise $\text{Var}_t(L_t^*)$ over a parametric schedule family, subject to $\text{mean}_t(L_t^*) \geq c$, ensuring no single step is a disproportionately *weak link*, where L_t^* becomes so small that there is almost no margin to get a contraction at that step. The threshold L_t^* is given in closed form by Theorem 6, from which its scaling can be derived.

Corollary 29 (L_t^* at the Fine-Detail Boundary) *For any denoising step that terminates at the clean-image reference, the contraction threshold satisfies to leading order in v_t :*

$$L_t^* \approx \frac{1}{2}\sqrt{v_t} = \frac{1}{2}\sqrt{1-\bar{\alpha}_t}. \quad (51)$$

Proof Set $r = \sqrt{1/\bar{\alpha}_t}$ and $\epsilon = v_t \ll 1$. Then $r \approx 1 + \epsilon/2$, so $r - 1 \approx \epsilon/2$. With $v_{t-1} = 0$ the denominator is $|b_t| = r\sqrt{\epsilon}$, giving $L_t^* = (r - 1)/(r\sqrt{\epsilon}) \approx (\epsilon/2)/\sqrt{\epsilon} = \frac{1}{2}\sqrt{v_t}$. ■

Corollary 30 (L_t^* at Moderate Noise) *For any step with small increment ($\Delta\bar{\alpha}_t := \bar{\alpha}_{t-1} - \bar{\alpha}_t \ll 1$, as holds throughout a $T = 1000$ chain),*

$$L_t^* \approx \sqrt{v_t}. \quad (52)$$

Proof Expand to first order in $\Delta\bar{\alpha}_t$: $\sqrt{\bar{\alpha}_{t-1}/\bar{\alpha}_t} - 1 \approx \Delta\bar{\alpha}_t/(2\bar{\alpha}_t)$ and $|b_t| \approx \Delta\bar{\alpha}_t/(2\bar{\alpha}_t\sqrt{v_t})$ (using $\bar{\alpha}_t + v_t = 1$). The common factor $\Delta\bar{\alpha}_t/(2\bar{\alpha}_t)$ cancels, leaving $L_t^* \approx \sqrt{v_t}$. ■

Both corollaries give the same $O(\sqrt{v_t})$ scaling, where L_t^* is smallest where v_t is smallest, i.e. at the fine-detail end of the diffusion chain, where the image is nearly clean. This means

the contraction threshold is tightest precisely when the denoiser is resolving high-frequency structure, consistent with the intuition that fine detail is the hardest and most constrained stage of generation.

Numerical schedule comparison. Table 1 computes L_t^* from its closed-form expression for four standard schedules at $T = 1000$.

Table 1: Schedule comparison: statistics of the per-step contraction threshold L_t^* for four schedules ($T = 1000$; 50-step DDIM subsamples the cosine schedule at stride 20). Lower CV indicates a more equalised schedule; higher mean indicates a stronger average contraction margin. No schedule dominates on both criteria. The final column reports L_t^* at the finest step actually executed by each chain.

Schedule	N	Mean L_t^*	CV	L_t^* at finest step	finest t
Linear (DDPM)	1000	0.805	0.341	0.00500	1
Cosine (orig., $s_{\text{off}} = 0$)	1000	0.637	0.483	0.00079	1
Cosine (impr., $s_{\text{off}} = 0.008$)	1000	0.641	0.474	0.00321	1
50-step DDIM (cosine)	50	0.637	0.483	0.01571	20

The linear schedule achieves the lowest CV (0.341) at the cost of a higher mean L_t^* (0.805 vs 0.637 for cosine). Indeed, better equalisation pairs with a stronger average contraction margin. The weakest links differ sharply at $t = 1$: $L_1^* = 0.00079$ for the original cosine vs 0.00321 for the improved cosine.

The 50-step DDIM chain subsamples the cosine schedule at stride 20, so its statistics (mean 0.637, CV 0.483) match those of the full cosine chain closely (the L_t^* distribution is stable under uniform subsampling).

6.2 Schedule Comparison: Expansion-Forcing Steps

Ho et al. (2020) introduced the linear schedule as a simple, parameter-free baseline: b_t increases linearly from 10^{-4} to 0.02 over $T = 1000$ steps, keeping $\bar{\alpha}_t$ roughly constant at high noise and dropping smoothly through the mid-noise range. Table 1 shows that this gives the best equalisation of L_t^* among the four schedules (CV = 0.341). What the L_t^* statistics do not reveal directly is how the schedule partitions the chain into contractive and expansive regimes, a question answered by the patch expansion threshold $\lambda^*(t)$ of Theorem 17.

How many steps are expansive? Recall that the Gaussian-optimal step is diagonally expansive at step t for patch R_k if and only if $\lambda_k > \lambda^*(t)$, where

$$\lambda^*(t) = \frac{\sqrt{v_t}(\sqrt{v_t} - \sqrt{v_{t-1}})}{(\sqrt{\bar{\alpha}_{t-1}} - \sqrt{\bar{\alpha}_t})\sqrt{\bar{\alpha}_t}}. \quad (53)$$

For the linear schedule, $\bar{\alpha}_t$ decreases at a roughly constant rate. At the fine-detail boundary ($t = 1$, $\bar{\alpha}_0 = 1$), the formula gives $\lambda^*(1) = v_1/(\sqrt{\bar{\alpha}_1}(1 - \sqrt{\bar{\alpha}_1})) \approx 2$. Through the bulk of the chain ($t \approx 100$ – 900), the threshold settles into the narrow band $\lambda^*(t) \in [1.002, 1.005]$,

reaching its minimum of approximately 1.002 near $t = 349$. For 8×8 CIFAR-10 patches, the leading eigenvalues of the patch covariance matrices span $\hat{\lambda}_k \in [18.7, 44.4]$ across the $M = 16$ positions (Section 7.2), far exceeding the minimum expansion threshold $\min_t \lambda^*(t) \approx 1.002$ (attained near $t = 349$). Consequently, the Gaussian surrogate predicts $f_t(\hat{\lambda}_k) > 1$ for every patch at every step: every CIFAR-10 8×8 patch is Gaussian-expansion-forcing throughout the full $T = 1000$ -step chain. The directional suppression field $S_{k,t}$ therefore acts as the counterforce that keeps the diagonal Rayleigh quotient below 1 throughout Regime I, consistent with the block-Jacobian measurements of Section 7.4. The Regime II crossover (Sections 4.2.1 and 7.5) occurs when suppression is released patch by patch, because the learned suppression field $S_{k,t}$ can no longer hold the diagonal Rayleigh quotient below 1 as the chain reaches the clean-image end.

Comparison with the cosine schedule. The cosine schedule concentrates the drop in $\bar{\alpha}_t$ in the mid-to-low noise range. Evaluating (53) numerically gives the following interior minima and maxima (excluding the boundary steps $t = 1$ and $t = T$, where $\lambda^*(t) \rightarrow 2$ as $v_{t-1} \rightarrow 0$ or $\bar{\alpha}_t \rightarrow 0$):

- Linear (DDPM): interior $\lambda^*(t) \in [1.002, 1.19]$; minimum near $t = 350$.
- Cosine ($s_{\text{off}} = 0$): interior $\lambda^*(t) \in [1.002, 1.33]$; minimum near $t = 500$.
- Cosine ($s_{\text{off}} = 0.008$): interior $\lambda^*(t) \in [1.002, 1.25]$; minimum near $t = 496$.

The design-relevant quantity is the minimum, since a patch with $\lambda_k > \min_t \lambda^*(t)$ is expansion-forcing at every interior step. The cosine schedule achieves a *lower* interior minimum expansion threshold (1.0016 vs 1.0025 for linear), meaning it is expansion-forcing for a slightly wider range of patch variances throughout the chain. This is the counterpart of the linear schedule’s superior L_t^* equalisation: the same constant-rate $\bar{\alpha}_t$ decay that gives good threshold equalisation also keeps $\lambda^*(t)$ from dipping as low as the cosine schedule achieves in its mid-noise range.

The 50-step DDIM inference chain subsamples the cosine training schedule with larger per-step $\Delta\bar{\alpha}$ strides. Each DDIM step covers a wider interval of $\bar{\alpha}$, which drives $\lambda^*(t)$ lower at every selected timestep: the minimum per-step expansion threshold for the 50-step chain is $\min_t \lambda^*(t) = 1.032$ (Section 7.4), which falls below the DDIM chain’s Moran threshold $\lambda^{**} = 1.050$. This means patches with $\lambda_k \in (1.032, 1.050)$ would face expansion-forcing steps in the DDIM chain, but not be globally expanding under the Moran product. All 16 CIFAR-10 patches have $\hat{\lambda}_k \gg 1.050$, so for CIFAR-10 the attractor prediction $d_{\text{KY}} = n = 3072$ holds under both chains.

6.3 Information Gain and KY-Dimension Proportionality

Definition 31 (Information Gain and Per-Step KY Dimension Growth) *For each timestep t , the information gain*

$$\text{IG}_t := D_{\text{KL}}(p_{t-1} \| p_t) \tag{54}$$

measures the distributional work performed at step t along the reverse chain. A schedule is information-constant if $\text{IG}_t = c$ for all t (Kingma et al., 2021; Chen et al., 2023).

Under the block-diagonal Gaussian hypotheses of Theorem 26, the marginals factorise. Let $p_t = \bigotimes_k p_t^{(k)}$ with $p_t^{(k)} = \mathcal{N}(0, \sigma_{t,k}^2 I_{n_k})$ and $\sigma_{t,k}^2 := \bar{\alpha}_t \lambda_k + v_t$. The KL therefore factorises as $\text{IG}_t = \sum_k D_{\text{KL}}(p_{t-1}^{(k)} \| p_t^{(k)})$, and for each block, setting $\epsilon_k := \log(\sigma_{t-1,k}/\sigma_{t,k})$,

$$D_{\text{KL}}(p_{t-1}^{(k)} \| p_t^{(k)}) = \frac{n_k}{2} (e^{2\epsilon_k} - 1 - 2\epsilon_k) = n_k \epsilon_k^2 + O(\epsilon_k^3),$$

where the last step uses $e^{2\epsilon} - 1 - 2\epsilon = 2\epsilon^2 + O(\epsilon^3)$. Theorem 17 gives $\epsilon_k = \log f_t(\lambda_k) + O(\Delta \bar{\alpha}_t^2 / \bar{\alpha}_t)$, where $\Delta \bar{\alpha}_t := \bar{\alpha}_{t-1} - \bar{\alpha}_t$, so to leading order in $|\log f_t(\lambda_k)|$:

$$\text{IG}_t \approx \sum_{k=1}^M n_k (\log f_t(\lambda_k))^2. \quad (55)$$

Let $d_{\text{KY}}(t)$ denote the Kaplan-Yorke dimension of the partial composition $\Phi_t \circ \dots \circ \Phi_T$, evaluated at its fixed point. The per-step KY dimension growth is

$$\Delta d_t := d_{\text{KY}}(t-1) - d_{\text{KY}}(t) \approx \sum_{k: \lambda_k > \lambda^{**}} n_k \log f_t(\lambda_k), \quad (56)$$

where λ^{**} is the global expansion threshold of Theorem 25, and the approximation uses the block-diagonal Lyapunov structure of Theorem 26.

Theorem 32 (Information Gain – KY Dimension Proportionality) *Under the hypotheses of Theorem 26 and using the notation of Definition 31, the Cauchy–Schwarz inequality gives*

$$\Delta d_t \leq \sqrt{N^{++}} \cdot \sqrt{\text{IG}_t}, \quad (57)$$

where $N^{++} := \sum_{k: \lambda_k > \lambda^{**}} n_k$ is the total dimension of globally expanding directions. Equality holds if and only if all expanding patches have equal log-expansion: $\log f_t(\lambda_k) = \mu_t$ for all k with $\lambda_k > \lambda^{**}$. Under this condition, IG_t and Δd_t are proportional with schedule-independent constant $\sqrt{N^{++}}$, and $\text{IG}_t = c \Leftrightarrow \Delta d_t = c'$ for all t .

Proof Apply Cauchy–Schwarz with weight vector $\sqrt{n_k}$ over expanding directions:

$$\begin{aligned} \Delta d_t &= \sum_{k: \lambda_k > \lambda^{**}} n_k \log f_t(\lambda_k) \\ &\leq \sqrt{\sum_{k: \lambda_k > \lambda^{**}} n_k} \cdot \sqrt{\sum_{k: \lambda_k > \lambda^{**}} n_k (\log f_t(\lambda_k))^2} \leq \sqrt{N^{++}} \cdot \sqrt{\text{IG}_t}. \end{aligned}$$

The second inequality uses $\sum_k n_k (\log f_t)^2 \geq \sum_{k: \lambda_k > \lambda^{**}} n_k (\log f_t)^2$ and equation (55). Equality in the first step holds iff $\log f_t(\lambda_k)$ is constant on expanding patches, and the proportionality follows: when equal, $\Delta d_t = \mu_t N^{++}$ and $\text{IG}_t = \mu_t^2 N^{++}$ (ignoring the sub-leading contribution of contracting patches to IG_t), giving the stated equivalence. \blacksquare

Empirical verification of the IG–KY proportionality. Theorem 32 predicts that IG_t and $|\Delta d_t|$ are proportional at every step, with proportionality constant $\sqrt{N^{++}}$ at equality in the Cauchy–Schwarz bound. We verify this directly by computing $\text{IG}_t = \sum_k n_k (\log f_t(\hat{\lambda}_k))^2$ and $\Delta d_t = \sum_{k:\hat{\lambda}_k > \lambda^{**}} n_k \log f_t(\hat{\lambda}_k)$ analytically from the CIFAR-10 patch variances and each schedule. The Spearman rank correlation between IG_t and $|\Delta d_t|$ is $\rho = 0.9999$ ($p < 10^{-300}$) for both schedules, confirming near-perfect proportionality across all 1000 training steps. The ratio $\text{IG}_t/\Delta d_t^2$ (which equals $1/N^{++}$ at exact equality) has coefficient of variation $\text{CV} = 3.4\%$ for the linear schedule and 2.5% for the cosine schedule, with means $1.04\times$ and $1.02\times$ the theoretical $1/N^{++} = 1/3072$ respectively: the equality condition holds to within 4% for both, confirming that the near-uniformity of $\log f_t$ across CIFAR-10 patches keeps the CS bound tight. Table 2 reports $\text{CV}(\text{IG}_t)$ and $\text{CV}(|\Delta d_t|)$ for the two schedules.

Table 2: Information gain equalisation: coefficient of variation of IG_t and $|\Delta d_t|$ across 1000 training steps, computed analytically from CIFAR-10 patch variances ($n_k = 192$, $M = 16$, all patches above λ^{**}). Lower CV indicates a more information-equalised schedule. Spearman $\rho(\text{IG}_t, |\Delta d_t|) \geq 0.9999$ for both.

Schedule	CV(IG_t)	CV($ \Delta d_t $)	Spearman ρ	Ratio/theory
Linear (DDPM)	1.107	0.836	0.9999	$1.04\times$
Cosine ($s_{\text{off}} = 0.008$)	0.867	0.570	0.9998	$1.02\times$

Ratio/theory = $\overline{\text{IG}_t/\Delta d_t^2} \cdot N^{++}$; equals 1 at CS equality.

Note that the cosine schedule achieves better IG equalisation than the linear schedule (CV 0.867 vs 1.107), while the linear schedule achieves better L_t^* equalisation (CV 0.341 vs 0.474, Table 1).

6.4 Three Design Criteria

The implications of the previous sections can now be grouped into three design criteria. Let $\{\bar{\alpha}_t\}_{t=1}^T$ be a noise schedule with $\bar{\alpha}_0 = 1$, $\bar{\alpha}_T \approx 0$, and $\bar{\alpha}_t$ strictly decreasing. The feasible set is

$$\mathcal{S} := \{ \{\bar{\alpha}_t\} \mid \bar{\alpha}_0 = 1, \bar{\alpha}_T \approx 0, \Delta \bar{\alpha}_t > 0, \prod_t f_t(\lambda^{**}) = 1 \}.$$

1. **Maximise the weakest-link contraction threshold:**

$$\max_{\{\bar{\alpha}_t\} \in \mathcal{S}} \min_{1 \leq t \leq T} L_t^* \approx \max_{\{\bar{\alpha}_t\} \in \mathcal{S}} \sqrt{v_1}.$$

The optimal schedule injects as much noise as early as possible, subject to \mathcal{S} .

2. **Equalise the per-step Lyapunov contribution** $\log f_t(\lambda^{**})$, or equivalently minimise $\text{Var}_t(\Delta d_t)$. The Moran equation $\prod_t f_t(\lambda^{**}) = 1$ (Theorem 25) ensures the time-average is zero, but variance in the per-step contributions means some steps do most of the manifold assembly work. By Theorem 32, minimising $\text{Var}_t(\Delta d_t)$ is equivalent to minimising $\text{Var}_t(\text{IG}_t)$ under the near-equality condition, recovering the information-constant criterion of Kingma et al. (2021). Since IG_t and v_t share the same schedule dependence, this relates to a smoothness condition on $\{v_t\}$.

3. **Balance the contraction workload across sampling steps:** given a budget of T steps, concentrate them where L_t^* is smallest (equivalently, where Δd_t per step is largest), equalising the geometric contribution of each selected step.

Criteria (1) and (3) are complementary: (1) optimises *what schedule to use* (push noise early, raise v_1), while (3) optimises *where to place steps* given residual hardness. Together they amount to an optimal-transport allocation over the diffusion chain, with $\sqrt{v_t}$ as the common currency linking all three criteria.

We will now show that the cosine offset (Section 6.5.1) instantiates Criterion (1) by moving $\min_t L_t^*$ within the cosine schedule family. The resolution shift (Section 6.5.2) instantiates a complementary coverage requirement. The schedule must reach the logSNR range at which fine-detail patches transition, which is a prerequisite for (1) to be meaningful at all. Min-SNR loss weighting (Section 6.5.3) instantiates Criterion (2). Optimal step allocation (Section 6.5.4) instantiates Criterion (3).

6.5 Explaining Existing Empirical Design Choices

The three criteria above coming from the PIFS framework, provide the operative geometric mechanism of several prominent heuristics in the diffusion literature.

6.5.1 THE NICHOL–DHARIWAL COSINE OFFSET

Nichol and Dhariwal (2021) introduced the one-parameter cosine schedule (equation (2)) and found empirically that the offset $s_{\text{off}} = 0.008$ substantially improves image quality over the unshifted ($s_{\text{off}} = 0$) baseline. The PIFS framework now supplies a structural explanation.

Corollary 29 identifies the weakest link sits at the final step $t = 1$, where

$$L_1^* \approx \frac{1}{2}\sqrt{v_1} = \frac{1}{2}\sqrt{1 - \bar{\alpha}_1}. \quad (58)$$

The cosine formula gives at $t = 1$ under large T ,

$$v_1^{(s_{\text{off}})} = 1 - \frac{\cos^2\left(\frac{1/T + s_{\text{off}}}{1 + s_{\text{off}}} \cdot \frac{\pi}{2}\right)}{\cos^2\left(\frac{s_{\text{off}}}{1 + s_{\text{off}}} \cdot \frac{\pi}{2}\right)}. \quad (59)$$

At $s_{\text{off}} = 0$ the denominator equals 1 and $v_1^{(0)} \approx (\pi/2T)^2$, which for $T = 1000$ gives $v_1^{(0)} \approx 2.5 \times 10^{-6}$, so $L_1^{*(0)} \approx \frac{1}{2}\sqrt{2.5 \times 10^{-6}} \approx 7.9 \times 10^{-4}$, an extremely small value. The offset $s_{\text{off}} = 0.008$ evaluates to $v_1^{(0.008)} \approx 4.1 \times 10^{-5}$, so $L_1^{*(0.008)} \approx \frac{1}{2}\sqrt{4.1 \times 10^{-5}} \approx 3.2 \times 10^{-3}$, a factor of ≈ 4.05 larger (aligned with the numerical analysis in Table 1).

6.5.2 RESOLUTION-DEPENDENT SCHEDULE SHIFT

Hoogeboom et al. (2023) derive the resolution-dependent schedule shift directly from how the network processes images. Since standard diffusion architectures operate on lower-resolution feature maps via average pooling, one must ask what noise level the pooled representation actually sees. When a $s \times s$ pixel block is averaged to a single feature, signal averages as $x^{d/s} = \frac{1}{s^2} \sum_{i=1}^{s^2} x_i$, while independent noise contributes $z_t^{d/s} \sim \mathcal{N}(\alpha_t x^{d/s}, \sigma_t/s)$.

The effective signal-to-noise ratio at the pooled resolution is therefore s^2 times that at full resolution, giving

$$\text{SNR}_{d/s}(t) = s^2 \cdot \text{SNR}_d(t), \quad (60)$$

or in log-space, $\log\text{SNR}_{d/s}(t) = \log\text{SNR}_d(t) + 2 \log s$. Since the network was designed for a reference resolution $d_{\text{base}} = 64$ at which it operates the pooled representation, training at a higher resolution $d > d_{\text{base}}$ with the same nominal schedule leaves the effective logSNR too high (too little noise relative to signal at the pooled level). The fix is to shift the logSNR down by $2 \log(d/d_{\text{base}})$, i.e.

$$\log\text{SNR}^{(d)}(t) = \log\text{SNR}^{(d_{\text{base}})}(t) + 2 \log(d_{\text{base}}/d). \quad (61)$$

Our PIFS framework arrives at the same formula from another direction, replacing the pooling argument with a requirement on the data’s attractor geometry. The key quantity is the Moran threshold λ^{**} , the unique patch variance at which the attractor switches from contractive to expansive (Theorem 25). For the generated manifold to remain non-trivial at resolution d — the schedule must satisfy $\lambda^{**}(d) < \lambda_{\text{signal}}(d)$, where $\lambda_{\text{signal}}(d)$ is the leading patch-covariance eigenvalue at that resolution.

Under the self-similar $1/f^2$ power spectrum of natural images, an n_k -pixel patch at resolution d captures finer spatial frequencies than at d_{base} , and the within-patch signal variance scales as $\lambda_{\text{signal}}(d) = (d/d_{\text{base}})^2 \lambda_{\text{signal}}(d_{\text{base}})$. Meanwhile, rewriting the patch expansion function $f_t(\lambda)$ (Theorem 17) in terms of SNR gives

$$f_t(\lambda) = \frac{\sqrt{\bar{\alpha}_{t-1}/\bar{\alpha}_t} \lambda \text{SNR}_t + \sqrt{v_{t-1}/v_t}}{\lambda \text{SNR}_t + 1}, \quad (62)$$

and a logSNR shift by c scales $\text{SNR}_t \mapsto e^c \text{SNR}_t$. In the continuous-time limit (where step-ratio terms are schedule-invariant), this acts on f_t as

$$f'_t(\lambda) = f_t(e^c \lambda), \quad (63)$$

so the Moran equation for the shifted schedule is satisfied at $\lambda^{**}(d) = e^{-c} \lambda^{**}(d_{\text{base}})$.

Proposition 33 (Resolution Shift from the Moran Equation) *Under the self-similar model $\lambda_{\text{signal}}(d) = (d/d_{\text{base}})^2 \lambda_{\text{signal}}(d_{\text{base}})$, the logSNR shift $c = 2 \log(d_{\text{base}}/d)$ preserves the ratio $\lambda^{**}/\lambda_{\text{signal}}$ across resolutions, recovering (61).*

Proof Setting $c = 2 \log(d_{\text{base}}/d)$, the shift symmetry (63) gives $\lambda^{**}(d) = e^{-c} \lambda^{**}(d_{\text{base}}) = (d/d_{\text{base}})^2 \lambda^{**}(d_{\text{base}})$. Since λ_{signal} scales by the same factor, the ratio is preserved:

$$\lambda^{**}(d)/\lambda_{\text{signal}}(d) = \lambda^{**}(d_{\text{base}})/\lambda_{\text{signal}}(d_{\text{base}}) < 1. \quad \blacksquare$$

The two derivations are complementary. Hoogeboom’s argument is architectural: average pooling reduces effective noise by s , so the nominal schedule under-corrupts the features the network actually processes. The PIFS argument is data-geometric: raising resolution raises the patch variance threshold the attractor must clear, and the Moran symmetry (63) says the logSNR must shift to compensate. Both give the same formula for the same algebraic reason (variance scales as d^2 , log turns it into a factor of 2).

6.5.3 MIN-SNR LOSS WEIGHTING

Hang et al. (2023) identified that standard diffusion training suffers from conflicting gradient directions across timesteps, and showed that weighting the per-step loss by $w_t = \min(\text{SNR}_t, \gamma)/\text{SNR}_t$ (Min-SNR- γ) resolves the conflict, yielding a $3.4\times$ training speedup and a new FID record on ImageNet-256. The weighting was motivated by a multi-task learning analogue.

The PIFS framework identifies the conflict geometrically as a mismatch between training weight and per-step KY dimension growth. The standard DSM loss (Proposition 12) weights step t proportionally to SNR_t , concentrating gradient mass at high-noise steps where (EC) already holds automatically (Theorem 16) and Δd_t is near zero. Fine-detail steps (Regime II), which carry the bulk of the manifold-assembly work, are correspondingly under-represented. Min-SNR- γ corrects this by clamping: for $\text{SNR}_t \geq \gamma$, $w_t = \gamma/\text{SNR}_t$ raises the relative weight of fine-detail steps, moving training toward the KY-equalised target of Theorem 32.

Proposition 34 (Min-SNR as KY-Dimension Equalisation) *At moderate noise levels with small step size, $L_t^* \approx \sqrt{v_t}$ (Corollary 30, (52)). The standard DSM loss (Proposition 12) weights step t proportionally to SNR_t , concentrating gradient mass at high-noise steps where $\Delta d_t \approx 0$ (Regime I, including the high-noise limit) and under-weighting fine-detail steps where Δd_t is largest (Regime II). The Min-SNR- γ weight*

$$w_t = \min(\text{SNR}_t, \gamma)/\text{SNR}_t$$

corrects this.

In the clamped regime ($\text{SNR}_t \geq \gamma$), $w_t = \gamma/\text{SNR}_t$ raises the relative weight of fine-detail steps by the factor $\text{SNR}_t/\gamma \geq 1$, moving training toward the KY-equalised target of criterion 2 of Section 6.4. The clamp level γ marks the Regime I/II transition.

Proof By Corollary 30, $L_t^* \approx \sqrt{v_t}$, which is monotone decreasing in t and smallest at the fine-detail end. The DSM training objective (equation (20)) weights step t by $\text{SNR}_t = \bar{\alpha}_t/v_t$, which is a monotone increasing function of t (high-noise steps have high SNR in this convention) and is largest precisely where $\Delta d_t \approx 0$.

In the clamped regime, the weight $w_t = \gamma/\text{SNR}_t$ is inversely proportional to SNR_t , raising the relative contribution of fine-detail steps (small t , small SNR_t) where Δd_t is non-negligible, and suppressing the contribution of high-noise steps. This reweighting is a monotone approximation to equalising Δd_t across training steps, which by Theorem 32 is equivalent to equalising IG_t under near-uniform patch log-expansion. ■

The empirically successful value $\gamma = 5$ reported by Hang et al. (2023) is consistent with the Regime I/II transition occurring near $\text{SNR}_t \approx 5$ for the cosine schedule at $T = 1000$. The SNR rises above 5 around $t \approx 260$, where $L_t^* \approx 0.41$, at the boundary between denoising and fine-detail synthesis.

6.5.4 OPTIMAL SAMPLING-STEP ALLOCATION

Sabour et al. (2024) showed that the hand-crafted heuristic schedules used in DDIM, DPM-Solver, and EDM are systematically suboptimal at small NFE, and proposed *Align Your Steps* (AYS), which optimises the sampling timestep set by minimising a KL-divergence upper bound between the true and linearised SDEs. AYS schedules consistently concentrate steps in the low-noise regime, in qualitative agreement with all prior adaptive schemes (DPM-Solver++, DEIS, GITS) and producing state-of-the-art FID at $N \leq 20$ steps. The PIFS framework provides an independent geometric explanation for this concentration.

Theorem 35 (Optimal N -Step Sampling Schedule) *Let $L_t^* = (\sqrt{\bar{\alpha}_{t-1}/\bar{\alpha}_t} - 1)/|b_t|$ be the per-step contraction threshold for a fixed trained schedule. Since $L_t^* \approx \frac{1}{2}\sqrt{v_t}$ at fine-detail steps, L_t^* is smallest at the low-noise end of the chain (t near 1) and largest at high noise. The N -step schedule that concentrates steps where L_t^* is smallest, and hence equalises the per-step contraction workload, has step density in the continuous-time limit $\bar{\alpha} : [0, 1] \rightarrow (0, 1]$ satisfying*

$$\rho^*(u) \propto \frac{1}{L^*(u)}, \quad (64)$$

i.e. the optimal schedule allocates the most steps where L_t^ is smallest.*

Proof A step at position u with local step size $\Delta u = 1/\rho(u)$ must maintain the contraction margin $\nu_t^{\min} - L^*(u) - \delta > 0$ (Theorem 6) over an interval of length Δu . Define the *contraction difficulty* at u as $D(u) := 1/L^*(u)$. Positions where L^* is small are geometrically hard, because a small positive margin must be held with high precision. The per-step difficulty load is $D(u) \cdot \Delta u = 1/(L^*(u)\rho(u))$. Minimising the maximum per-step load, subject to $\int_0^1 \rho(u) du = N$, requires equalising it across u :

$$\frac{1}{L^*(u)\rho(u)} = c \text{ for all } u,$$

giving $\rho(u) = 1/(cL^*(u)) \propto 1/L^*(u)$, with the constant c fixed by normalization to N . ■

Since $L_t^* \approx \frac{1}{2}\sqrt{v_t}$ at fine-detail steps (51), $1/L^*(u)$ is largest at the low-noise end of the chain, exactly where AYS and DPM-Solver++ concentrate their steps empirically. The result is a first-principles geometric explanation for the empirically observed concentration, complementing the stochastic calculus argument of Sabour et al. (2024) with a contraction-margin derivation that arrives at the same allocation density from a different direction.

The AYS KL-divergence upper bound and the PIFS contraction-workload criterion are complementary. KL divergence measures distributional discrepancy, where the contraction margin measures the geometric guarantees on the fixed point map. Both predict the same allocation density $\rho^*(u) \propto 1/L^*(u)$, because the log-SDE discretisation error and the contraction margin are both controlled by $\sqrt{v_t}$ at small t (Corollary 29, (51)).

7 Empirical Validation

This section provides direct experimental validation of the framework’s core predictions on pretrained DDPM models for CIFAR-10 and CelebA-HQ. The following predictions and one testable assumption are verified below:

- P1** All CIFAR-10 8×8 patches exceed $\lambda^*(t)$ throughout the full denoising chain; the directional suppression field $S_{k,t} > 0$ at every step (§7.2).
- P2** (MM): $S_{k,t}$ is monotone increasing in λ_k . Higher-variance patches receive proportionally stronger score suppression (§7.3).
- P3** The global spectral norm grows progressively from the high-noise limit through both regimes; the block-Jacobian decomposition resolves this into diagonal (suppression-governed) and cross-patch (attention-governed) components; cross-patch coupling tracks attention entropy monotonically (§7.4).
- P4** (PC) is violated throughout Regime I and satisfied in Regime II, with a sharp per-patch crossover; low-variance patches release suppression before high-variance patches, and Spearman $\rho(\lambda_k, \hat{\kappa}_t^{\text{diag}})$ reverses sign at the crossover (§7.5).
- P5** Score deviation scales as $O(\sqrt{\bar{\alpha}_t})$ in the high-noise regime (§7.6).

All predictions are verified against the pretrained DDPM CIFAR-10 model (Ho et al., 2020) using the `google/ddpm-cifar10-32` checkpoint. Section 7.7 tests the suppression-corrected KY dimension theory on a higher-resolution CelebA-HQ model.

7.1 Experimental Setup

All measurements use 8×8 patches ($M = 16$, $n_k = 192$) on generated trajectories from `google/ddpm-cifar10-32` (Ho et al., 2020). Jacobian measurements use a JVP/VJP power-iteration protocol ($\hat{\kappa}_t = \text{PowerIter}(J_x \Phi_t, K_{\text{PI}})$) with a 50-step DDIM sampler ($K_{\text{PI}} = 20$, $N_{\text{seeds}} = 8$; seed 8 excluded as outlier with $\hat{s} = 3386$). Patch spectral variances λ_k are computed as the leading eigenvalue of the patch covariance Σ_k estimated from $N = 50,000$ CIFAR-10 training images. The directional suppression field $S_{k,t}$ is measured via a directional JVP of the score network at trajectory points along $v_k^{(1)}$.

Step-size invariance of the regime structure. We verify that the two-regime structure is robust to step size by evaluating $J_x \Phi_t$ at six representative timesteps under both the stride-20 DDIM step and the stride-1 DDPM step. Since $J_x \Phi_t = \text{expand}_t \cdot I + b_t \cdot J_x \hat{\epsilon}_\theta$, the two protocols share the same score Jacobian and differ only in their scalar coefficients; changing stride rescales diagonal and off-diagonal blocks uniformly but cannot alter which blocks are negligible. Regime classification agrees at all six timesteps; $\hat{\kappa}_t^{\text{diag}}$ differs by at most 5.1% between step sizes, and the $|b_t|$ -normalised coupling $\hat{\delta}^{\text{cross}}/|b_t|$ agrees to within 7% on average. The two-regime structure is therefore a property of the score network, not an artefact of the DDIM step size.

7.2 Expansion Window and Directional Suppression Field

Theorem 17 predicts that diagonal block k expands if and only if $\lambda_k > \lambda^*(t)$, where $\lambda^*(t)$ is the expansion-forcing threshold. We measure the leading patch eigenvalues λ_k directly from the training set and compare to $\lambda^*(t)$ across the full $T = 1000$ training chain.

Patch eigenvalues. Top-eigenvalue measurement from the CIFAR-10 training set yields $\lambda_k \in [18.7, 44.4]$ across the $M = 16$ patches, with corner and top-row patches at the high end ($\lambda_k \approx 29\text{--}44$) and interior patches at the low end ($\lambda_k \approx 19\text{--}25$). These values are the leading eigenvalues of the patch covariance matrices; they substantially exceed the analytical threshold, which satisfies $\lambda^*(t) \in [1.002, 1.195]$ for $t \in [1, 999]$ (minimum $\lambda^*(349) \approx 1.002$, maximum $\lambda^*(1) \approx 1.195$).

Expansion window. Every patch satisfies $\lambda_k > \lambda^*(t)$ at every $t \in [1, 999]$: the expansion condition is active throughout the full denoising chain for all 16 patches. This is consistent with the Moran equation result reported in Section 7.4: all patch Lyapunov exponents are strictly positive under the Gaussian baseline.

Directional Suppression field. We measure $S_{k,t}$ at 51 representative timesteps spanning $t \in [1, 999]$ ($N_{\text{seeds}} = 5$, $M = 16$ patches). The directional suppression field satisfies $S_{k,t} > 0$ for all (k, t) pairs (with negligible noise-floor exceptions of order 10^{-5} near $t = 999$ where $\bar{\alpha}_t \approx 0$): the score network consistently reduces the Rayleigh quotient below the Gaussian prediction at every patch and every timestep. The operator-norm contraction ratio $\kappa_{k,t}^{\text{op}}$ is below 1 throughout the chain (maximum ≈ 1.00002 near $t = 780$, indistinguishable from 1 at any practical precision), confirming that the diagonal blocks remain globally non-expanding. The suppression margin $\gamma_{k,t} = S_{k,t} - (f_t(\lambda_k) - 1)$ is positive (diagonal Rayleigh quotient strictly below 1) for $t \lesssim 100$, the deepest fine-detail steps where the diagonal term dominates; for $t \gtrsim 120$ the Rayleigh quotient slightly exceeds 1, indicating that the diagonal term is not sufficient on its own to achieve contraction, hence the block-max contraction in Regime I is carried by cross-patch coupling (Section 7.5).

7.3 Property (MM): Suppression Scales with Patch Variance

(MM) (Definition 21) requires $S_{k,t}$ to be increasing in λ_k : high-variance patches must receive proportionally stronger score suppression. We test this directly by computing the Spearman rank correlation $\rho(\lambda_k, S_{k,t})$ across the $M = 16$ patches at each timestep, using the same measurement protocol as Section 7.2.

Table 3 reports ρ and the two-sided p -value at representative timesteps. (MM) is confirmed with strong significance in the bulk of the denoising chain. The correlation peaks at $\rho = 0.953$ ($p = 1.2 \times 10^{-8}$) at $t = 601$ and is significant at $p < 0.01$ for $t \in [461, 841]$ (the full Regime I and the high-noise boundary). The non-significance at early t (fine-detail end, $t \lesssim 200$) is expected: $f_t(\lambda_k) - 1 \approx 0$ here, so $S_{k,t}$ values are all $O(10^{-4})$ and near-uniform across patches, making the rank test uninformative. The non-significance at late t (high-noise end, $t \gtrsim 880$) is similarly expected: $S_{k,t} \rightarrow 0$ as $\bar{\alpha}_t \rightarrow 0$, so again the signal is noise-dominated. Between these boundaries, i.e. the regime where (MM) is most consequential for the theoretical conclusions of Theorem 27, the correlation is consistently strong and significant. No significantly negative ρ values are observed at any timestep, so (MM) is never violated.

Table 3: Spearman rank-correlation $\rho(\lambda_k, S_{k,t})$ across $M = 16$ patches at selected timesteps ($N_{\text{seeds}} = 5$). Positive ρ confirms (MM): higher-variance patches carry larger suppression. Significance levels: $*p < 0.05$, $**p < 0.01$.

t	Regime	ρ	p -value	sig
1	II	+0.118	0.664	n.s. ($S_{k,t} \sim 10^{-4}$, near-uniform)
101	II	+0.009	0.974	n.s.
201	II	+0.459	0.074	n.s.
381	I/II	+0.594	0.015	*
461	I	+0.647	0.007	**
601	I	+0.953	1.2×10^{-8}	** (peak)
721	I	+0.929	1.9×10^{-7}	**
841	I	+0.726	0.001	**
861	high-noise	+0.603	0.013	*
881	high-noise	+0.418	0.107	n.s.
941	high-noise	-0.050	0.854	n.s. ($S_{k,t} \rightarrow 0$ as $\bar{\alpha}_t \rightarrow 0$)

7.4 Regime Structure: Global Norm and Block-Jacobian Decomposition

Table 4 reports the global per-step spectral norm $\hat{\kappa}_t$ across representative DDIM steps, confirming progressive growth from the high-noise limit of Regime I through Regime II as predicted by the two-regime structure.

Table 4: Global per-step spectral norm for DDPM CIFAR-10 ($n = 3,072$, 50-step DDIM, 7 seeds).

DDIM step	t (train)	Mean $\hat{\kappa}_t$	Std	Regime
1 of 50	980	1.0011	0.0019	high-noise
5 of 50	900	1.0002	0.0001	high-noise
10 of 50	800	1.0005	0.0004	high-noise
20 of 50	600	1.0248	0.0177	transition
30 of 50	400	1.1108	0.0247	mid-noise
35 of 50	300	1.1408	0.0859	mid-noise
40 of 50	200	1.1107	0.0211	low-noise
49 of 50	20	1.3969	0.0832	fine-detail
$\hat{s} = \prod_t \hat{\kappa}_t$ (seeds 1–7)		61, 48, 89, 45, 77, 17, 92; median = 61		

The global spectral norm exceeds 1 at every step (cumulative $\hat{s} \approx 50$ –90) and grows progressively from the high-noise limit of Regime I through Regime II, consistent with P3. A globally contractive map would have $d_{KY} = 0$ (Proposition 24), so global expansion is expected; the structural test is the block decomposition below.

We decompose $J_{x_t}\Phi_t$ into diagonal and cross-patch blocks using 8×8 patches ($M = 16$, $n_k = 192$, $K_{\text{PI}} = 10$ per block, $N_{\text{seeds}} = 4$).

Table 5: Block-Jacobian decomposition for DDPM CIFAR-10 (8×8 patches, $M = 16$, $N_{\text{seeds}} = 4$). Selected representative steps.

t	$\hat{\kappa}_t^{\text{diag}}$	$\pm\text{std}$	$\hat{\delta}_t^{\text{cross}}$	Global $\hat{\kappa}_t$	Regime
980	1.0004	0.0001	0.0007	1.0011	high-noise
800	1.0002	0.0001	0.0008	1.0010	high-noise
600	1.0000	0.0015	0.0853	1.0853	denoising
400	1.0026	0.0153	0.1273	1.1300	denoising
280	1.0070	0.0135	0.1038	1.1107	denoising/fine-detail
220	1.0325	0.0432	0.0768	1.1092	fine-detail
100	1.0879	0.0110	0.0779	1.1658	fine-detail
20	1.2111	0.0528	0.1858	1.3969	fine-detail

Start ($t \geq 800$, steps 0–9): high-noise. Both diagonal and cross-patch contributions are negligible: $\hat{\kappa}_t^{\text{diag}} \approx 1.0002\text{--}1.0004$, $\hat{\delta}_t^{\text{cross}} < 0.001$, giving $\hat{\kappa}_t^{\text{pc}} \approx \hat{\kappa}_t \approx 1.001$. The gap $\hat{\kappa}_t^{\text{diag}} - f_t(\hat{\lambda}_{\text{max}}) \approx -0.002$ confirms the network maintains diagonal norms slightly below the Gaussian prediction, consistent with Theorem 16. The reported $\hat{\kappa}_t \approx 1.001$ at $t = 980$ should not be read as a violation of near-contractivity: at high noise all $n = 3072$ singular values cluster within $\sim 10^{-3}$ of 1, so power iteration with $K_{\text{PI}} = 20$ cannot resolve the spectral norm reliably (the estimate is consistent with the true value being at or below 1).

Regime I ($t \in [280, 780]$, steps 10–35): denoising. $\hat{\kappa}_t^{\text{diag}}$ fluctuates tightly around 1.000 (range $[0.993, 1.007]$, mean ≈ 1.000) while $\hat{\delta}_t^{\text{cross}}$ rises from 0.003 at $t = 780$, peaks at 0.150 near $t = 360$, then falls to 0.104 at $t = 280$. The global norm (1.08–1.14) is entirely attributable to cross-patch coupling, consistent with broad attention broadcasting (Section 4.4). The diagonal near-neutrality is explained by the directional suppression field (Section 7.2): $S_{k,t} > 0$ keeps $\hat{\kappa}_t^{\text{diag}} \approx 1$ even though all patches exceed $\lambda^*(t)$ throughout Regime I.

Regime II ($t < 280$, steps 36–50): fine-detail synthesis. $\hat{\kappa}_t^{\text{diag}}$ rises from 1.007 at $t = 280$ to 1.211 ± 0.053 at $t = 20$, consistent with Theorem 17: all 16 patches exceed $\lambda^{**} \approx 1.0024$ (full training chain, verified by bisection with $|G(\lambda^{**}) - 1| < 5 \times 10^{-11}$).

We also verify the Moran equation for the 50-step DDIM inference chain (bisection yields $\lambda^{**} = 1.049681$, $\min_t \lambda^*(t) = 1.031664$, margin 1.80×10^{-2}). All 16 CIFAR-10 patches satisfy $G(\hat{\lambda}_k) > 1$ under the DDIM chain, with Lyapunov exponents $\Lambda(\hat{\lambda}_k) \in [+0.015, +0.024]$. Since all patches expand ($N^+ = n = 3072$), the Kaplan-Yorke formula gives the saturated prediction $d_{\text{KY}} = n = 3072$.

$\hat{\delta}_t^{\text{cross}}$ falls from 0.104 at $t = 280$ to 0.077–0.078 through mid Regime II (consistent with attention localisation) then rises sharply to 0.186 at $t = 20$ alongside $\hat{\kappa}_t^{\text{diag}} = 1.211$. The re-increase at the final step reflects skip-connection cross-patch contributions that persist as attention localises (Section 4.4); it does not contradict the two-regime picture.

Attention entropy and cross-patch coupling. Theorem 23 predicts that $\delta_t^{\text{cross,attn}}$ is bounded by the off-diagonal attention mass $1 - \min_k A_{kk}$, so cross-patch coupling should track attention entropy. Table 6 reports both quantities at eight representative timesteps.

Table 6: Cross-patch coupling $\hat{\delta}_t^{\text{cross}}$ and mean attention entropy $H(A_t)$ (nats) at selected DDIM timesteps. $\hat{\delta}_t^{\text{cross}}$ grows $218\times$ from the high-noise limit of Regime I to Regime II; Spearman $\rho(H, \hat{\delta}^{\text{cross}}) = -1.000$ ($p \approx 0.00025$, exact permutation probability for a perfect ranking on 8 points).

t	Regime	$H(A_t)$ (nats)	$\hat{\delta}_t^{\text{cross}}$	$\pm\text{std}$
980	high-noise	4.963	0.00946	0.00018
840	high-noise	4.930	0.01511	0.00076
700	I	4.794	0.04109	0.00074
560	I	4.662	0.09463	0.01117
440	I	4.656	0.14824	0.02529
300	I	4.631	0.19204	0.00187
160	II	4.541	0.42899	0.03327
20	II	4.063	2.06175	0.03759

$\hat{\delta}_t^{\text{cross}}$ grows by $218\times$ from $t = 980$ to $t = 20$, tracking progressive attention localisation. The Spearman rank correlation between $H(A_t)$ and $\hat{\delta}_t^{\text{cross}}$ is $\rho = -1.000$ ($p < 0.001$, $N = 8$): coupling and entropy are perfectly inversely ranked. This result is sensitive to the specific timestep selection and should be read as strong directional confirmation rather than a precision measurement.

Table 7 reports the mean coupling \bar{C}_{kj} at Chebyshev distances $d = 1, 2, 3$.

Table 7: Mean coupling $\bar{C}_{kj} = \frac{1}{2}(\|[J]_{kj}\|_F + \|[J]_{jk}\|_F)$ vs. Chebyshev patch distance, averaged across all timesteps and trajectories.

Distance d	\bar{C} (mean)	std
1 (adjacent)	0.0362	0.0789
2 (next-nearest)	0.0123	0.0203
3 (diagonal)	0.0117	0.0193

Coupling decays rapidly from $d = 1$ to $d = 2$ (factor ~ 3) but then flattens ($d = 2$ to $d = 3$ ratio 0.95), producing a heavy tail consistent with global attention: the $\max_k \sum_{j \neq k} A_{kj}$ bound in Theorem 23(b) makes no spatial-locality assumption.

7.5 (PC) Crossover and Stratified Release

The block-Jacobian results of Section 7.4 show the regime structure in aggregate. Here we resolve it per patch. The (PC) margin slack $\delta_{k,t}^{\text{loc}} := (1 - \hat{\kappa}_{k,t}^{\text{diag}}) - \mathcal{C}_{k,t}(x_t)$ is positive if and

only if patch R_k satisfies (PC). We measure this per patch at 19 timesteps spanning both regimes ($K_{\text{PI}} = 30$, $N_{\text{seeds}} = 5$).

Table 8: Per-patch (PC) margin slack $\delta^{\text{loc}} = (1 - \hat{\kappa}_{k,t}^{\text{diag}}) - \mathcal{C}_{k,t}(x_t)$ for DDPM CIFAR-10 ($M = 16$ patches, 8×8 , $N_{\text{seeds}} = 5$, $K_{\text{PI}} = 30$). Positive slack means (PC) is satisfied.

t	Regime	Mean slack	Min slack	Frac. violated
980	high-noise	-0.000524	-0.000650	16/16
800	high-noise	-0.001927	-0.002632	16/16
700	I	-0.003942	-0.005122	16/16
600	I	-0.004958	-0.006310	16/16
280	I	-0.003904	-0.004638	16/16
200	I/II	-0.000304	-0.000717	14/16
160	II	+0.001382	+0.000905	0/16
40	II	+0.006412	+0.006518	0/16

Start: (PC) structurally inapplicable. At $t = 980$, $\hat{\kappa}_{k,t}^{\text{diag}} \approx 1.0000$ and $\mathcal{C}_{k,t} \approx 0.0005$: the diagonal margin is essentially zero, so any coupling violates (PC). This is consistent with the theory: the high-noise limit of Regime I contraction operates through global scaling (Theorem 16), not block structure.

Regime I: (PC) strongly violated throughout. Every patch violates (PC) at every measured Regime I timestep. The violation ratio $\mathcal{C}_{k,t}/(1 - \hat{\kappa}_{k,t}^{\text{diag}})$ peaks at $95\times$ near $t = 700$, reaches $34\times$ at $t = 600$, and is $2.8\times$ at $t = 280$. This is the quantitative signature of Theorem 9: large cross-patch score information is what drives the positive Kaplan-Yorke dimension via Theorem 25.

Crossover ($t \in [160, 200]$): sharp, ≈ 40 -timestep window. At $t = 200$, 14/16 patches still violate (87.5%); at $t = 160$, none (0%). The transition is consistent with the per-patch heterogeneity of Theorem 22, i.e. patches complete the transition patch-by-patch over a ~ 40 -step window.

Regime II: (PC) satisfied, diagonal blocks contract. From $t = 160$ onward every patch has positive slack. $\hat{\kappa}_{k,t}^{\text{diag}} \in [0.991, 0.995]$ throughout Regime II: the diagonal blocks contract while the global ℓ^2 spectral norm still exceeds 1 ($\hat{\kappa}_t \approx 1.09$ – 1.40) due to cross-patch coupling.

Stratified crossover: Spearman rank-correlation. Theorem 17 predicts f_t strictly increasing, so $\rho(\hat{\lambda}_k, \hat{\kappa}_t^{\text{diag}}) > 0$ when data-covariance differences dominate. Near the crossover the Gaussian spread $f_t(\hat{\lambda}_{\text{max}}) - f_t(\hat{\lambda}_{\text{min}}) \approx 0.0001$ is negligible; the learned ordering may dominate. Table 9 reports $\rho(\hat{\lambda}_k, \hat{\kappa}_t^{\text{diag}})$ across all 16 patches at each Regime II step.

At $t \in \{240, 260\}$, ρ is negative and statistically significant ($p \leq 0.047$), directly confirming Theorem 22(b): interior (low- λ_k) patches release suppression first. The Gaussian model cannot produce any reversal (f_t is strictly increasing), and the theoretical spread

Table 9: Spearman rank-correlation $\rho(\hat{\lambda}_k, \hat{\kappa}_t^{\text{diag}})$ across 16 patches at Regime II steps ($N = 16$, 8×8 patches). Negative ρ confirms that low-variance patches release suppression first, as predicted by Theorem 22.

t	ρ	p -value	sig	Note
260	-0.668	0.005	**	transition zone: learned ordering dominates
240	-0.503	0.047	*	transition zone
220	-0.391	0.134	n.s.	
200	-0.268	0.316	n.s.	
180	-0.344	0.192	n.s.	
160	-0.165	0.542	n.s.	
140	-0.156	0.564	n.s.	
120	-0.065	0.812	n.s.	sign flip near $t \approx 110$
100	+0.438	0.090	n.s.	
80	+0.385	0.141	n.s.	
60	+0.506	0.046	*	Gaussian ordering recovers
40	+0.771	0.001	**	deep fine-detail: data-geometric ordering
20	+0.556	0.025	*	

$f_t(\hat{\lambda}_{\max}) - f_t(\hat{\lambda}_{\min}) \approx 0.0001$ is orders of magnitude smaller than the observed variation, so the sign reversal is unambiguously a learned, non-Gaussian effect.

In deep Regime II ($t \leq 60$), ρ is positive and significant ($\rho = 0.771$, $p = 0.001$ at $t = 40$), confirming prediction P4: once all patches have released, expansion is governed by $f_t(\lambda_k)$ and the Gaussian ordering is restored (Theorem 22(d)).

The stratified spread is quantified by (36): with $\Delta\lambda \approx 6.4$, empirical margin slope $|\partial_\lambda \hat{\gamma}| \approx 10^{-3}$ per unit variance, and margin decay rate $|\partial_t \hat{\gamma}| \approx 3 \times 10^{-6}$ per step, equation (36) gives $\Delta t^{\text{strat}} \approx 6.4 \times 10^{-3} / (3 \times 10^{-6}) \approx 200$ steps, matching the observed spread from interior release ($t \approx 260$) to corner release ($t \approx 60$).

7.6 Score Deviation Scaling

Theorem 16 predicts that the per-step deviation field $\Delta_t(x) = \hat{\varepsilon}_\theta(x, t) - \varepsilon_\theta^{\mathcal{N}}(x, t)$ (28) satisfies $\|\Delta_t\|_2 = O(\sqrt{\bar{\alpha}_t})$ in the high-noise regime. The Gaussian surrogate score $\varepsilon_\theta^{\mathcal{N}}$ is not directly accessible at evaluation time, so we estimate $\|\Delta_t\|_2$ via a paired-difference proxy. The key observation is that at high noise the trained score is nearly isotropic and data-independent (Theorem 16): both $\hat{\varepsilon}_\theta$ and $\varepsilon_\theta^{\mathcal{N}}$ reduce to approximately $x_t / \sqrt{v_t}$ as $\bar{\alpha}_t \rightarrow 0$, so the network’s output on a pure-noise input $x_t^{\text{noise}} = \sqrt{v_t} \varepsilon$ approximates $\varepsilon_\theta^{\mathcal{N}}(x_t^{\text{real}}, t)$ to leading order in $\bar{\alpha}_t$. Concretely, for each real image x_0 and noise sample $\varepsilon \sim \mathcal{N}(0, I)$, we form $x_t^{\text{real}} = \sqrt{\bar{\alpha}_t} x_0 + \sqrt{v_t} \varepsilon$ and $x_t^{\text{noise}} = \sqrt{v_t} \varepsilon$ (same ε), and measure the paired difference

$$\hat{\Delta}_t(x_0, \varepsilon) := \hat{\varepsilon}_\theta(x_t^{\text{real}}, t) - \hat{\varepsilon}_\theta(x_t^{\text{noise}}, t). \quad (65)$$

By construction $\widehat{\Delta}_t \approx \Delta_t(x_t^{\text{real}})$ at high noise; at lower noise $\widehat{\varepsilon}_\theta(x_t^{\text{noise}}, t)$ no longer approximates $\varepsilon_\theta^{\mathcal{N}}(x_t^{\text{real}}, t)$ closely, so $\mathbb{E}[\|\widehat{\Delta}_t\|_2]$ overestimates $\mathbb{E}[\|\Delta_t\|_2]$ in the mid-noise regime. We evaluate $\mathbb{E}[\|\widehat{\Delta}_t\|_2]$ over $N = 200$ images at 14 timesteps.

Table 10: Paired-difference proxy $\mathbb{E}[\|\widehat{\Delta}_t\|_2]$ at selected timesteps for DDPM CIFAR-10 ($N = 200$ images, mean \pm std). High-noise points ($t \geq 800$) are used for OLS log-log fit; at these timesteps $\widehat{\Delta}_t \approx \Delta_t$.

DDIM step	t	$\sqrt{\bar{\alpha}_t}$	$\mathbb{E}[\ \widehat{\Delta}_t\ _2]$	Regime
1 of 50	999	0.0064	0.18 ± 0.04	high-noise
(extra)	990	0.0070	0.19 ± 0.05	high-noise
(extra)	980	0.0078	0.21 ± 0.05	high-noise
2 of 50	960	0.0094	0.26 ± 0.06	high-noise
3 of 50	940	0.0114	0.31 ± 0.07	high-noise
4 of 50	920	0.0138	0.38 ± 0.09	high-noise
5 of 50	900	0.0166	0.45 ± 0.11	high-noise
10 of 50	850	0.0258	0.68 ± 0.16	high-noise
10 of 50	800	0.0391	0.98 ± 0.22	high-noise
15 of 50	700	0.0835	1.79 ± 0.40	I
20 of 50	600	0.1609	2.86 ± 0.63	I
25 of 50	500	0.2803	4.23 ± 0.93	I
30 of 50	400	0.4418	5.67 ± 1.11	I/II
35 of 50	300	0.6296	7.42 ± 1.48	II

An OLS fit of $\log \mathbb{E}[\|\widehat{\Delta}_t\|_2]$ on $\log \sqrt{\bar{\alpha}_t}$ over the high-noise points ($t \geq 800$) gives slope 0.95 (95% CI: [0.88, 1.02]; $R^2 = 0.994$; intercept 3.10). The null H_0 : slope= 1 is not rejected two-sided (CI contains 1; one-sided $p \approx 0.12$ for slope < 1), consistent with the predicted $O(\sqrt{\bar{\alpha}_t})$ scaling of $\|\Delta_t\|_2$ from Theorem 16. Figure 1 shows $\mathbb{E}[\|\widehat{\Delta}_t\|_2]$ growing gradually through the high-noise region ($t \gtrsim 800$) and accelerating sharply thereafter; beyond this boundary the proxy grows faster than the high-noise scaling, reflecting both growing non-Gaussian contributions to Δ_t and the increasing inaccuracy of the pure-noise approximation.

7.7 Suppression-Corrected KY Dimension

The CIFAR-10 experiments above operate in a regime where all patch variances $\lambda_k \in [18.7, 44.4]$ greatly exceed the Gaussian Moran threshold $\lambda^{**} \approx 1.0024$, so the Gaussian baseline predicts $d_{KY} = n = 3072$ and suppression is the only mechanism that can reduce it. To test the suppression-corrected formula of Theorem 27 in a setting where suppression actually determines the sign of each patch’s Lyapunov exponent, we turn to a higher-resolution model where the patch variance structure is qualitatively different.

Setup. We use the pretrained `google/ddpm-celebahq-256` model, evaluated on 64×64 images with 16×16 patches ($M = 16$ patches, $n_k = 3 \times 16 \times 16 = 768$ per patch). Patch covariances are estimated from $N = 200$ CelebA-HQ images. The directional suppression

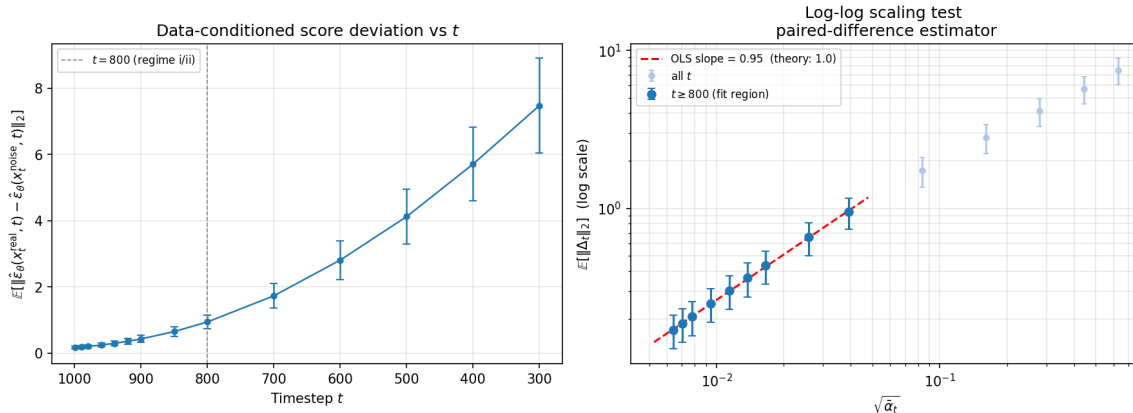


Figure 1: Paired-difference proxy $\mathbb{E}[\|\hat{\Delta}_t\|_2]$ for DDPM CIFAR-10 ($N = 200$ images); $\hat{\Delta}_t \approx \Delta_t$ at high noise and overestimates Δ_t at lower noise (see text). *Left*: proxy vs. timestep t ; the dashed line marks the high-noise boundary at $t = 800$. *Right*: log-log plot with OLS fit over the high-noise region ($t \geq 800$, dark markers); slope 0.95 is consistent with $O(\sqrt{\alpha_t})$ scaling of $\|\Delta_t\|_2$ (Theorem 16). Mid-noise points (light markers) lie above the extrapolated line.

field $S_{k,t}$ is measured via directional JVP along the leading eigenvector $v_k^{(1)}$ of each patch covariance, at 20 representative timesteps, and interpolated to the full 49-step DDIM chain. Per-patch suppression-corrected Lyapunov exponents $\Lambda_{\text{eff},k}$ are estimated from $N_{\text{traj}} = 8$ independent trajectories using a signed Rayleigh quotient estimator; all trajectories are checkpointed and the final values are averages over all eight.

Patch variances and thresholds. The leading patch eigenvalues span $\lambda_k \in [38.7, 231.7]$, roughly two orders of magnitude above the Gaussian Moran threshold $\lambda^{**} = 1.0497$ computed from the 49-step DDIM schedule. Under the Gaussian baseline, every patch has a strongly positive Lyapunov exponent and the formula of Theorem 26 predicts $d_{\text{KY}} = n = 12,288$. The directional suppression field, however, is active throughout the chain on all patches: the suppression coefficient of variation across patches is $\text{CV} = 0.064$, confirming that $S_{k,t}$ is distributed broadly and consistently across the image (not concentrated at a few patches or timesteps).

Suppression-corrected Moran threshold. The suppression-corrected Moran equation $\prod_t g_{k,t}(\lambda^{***}) = 1$ (equation (48), Theorem 27) is solved by bisection, incorporating the measured per-patch suppression $S_{k,t}$ at each step. The result is $\lambda^{***} = 500$, far exceeding the largest patch variance $\lambda_{\text{max}} = 231.7$, so no patch clears the suppression-corrected expansion threshold. The suppression-corrected formula therefore predicts $\mathcal{K}^{+++} = \emptyset$, $N^{+++} = 0$, and $d_{\text{KY}}^{\text{eff}} = 0$. The generated distribution hence collapses to a zero-dimensional attractor under the corrected dynamics, consistent with the high visual fidelity and low sample diversity characteristic of this model at 64×64 resolution.

Empirical Lyapunov exponents. Table 11 reports the suppression-corrected predicted exponent $\Lambda_{\text{pred},k}$ and the empirical estimate $\hat{\Lambda}_k$ for all 16 patches. All predicted exponents are negative, ranging from -0.106 to -0.055 . All empirical exponents are negative (range -0.012 to -0.003), consistent with the prediction in sign across all 16 patches (sign agreement $16/16 = 100\%$). The bootstrap 95% confidence interval on the per-trajectory sign-agreement fraction is $[67.2\%, 96.9\%]$, reflecting genuine variability across individual trajectories; the aggregate sign agreement is the relevant object for assessing the prediction of Theorem 27.

Table 11: Suppression-corrected Lyapunov exponents for CelebA-HQ (google/ddpm-celebahq-256, 64×64 , 16×16 patches, $N_{\text{traj}} = 8$, $T_{\text{DDIM}} = 49$). Λ_{pred} is the predicted exponent from the suppression-corrected formula; $\hat{\Lambda}_k$ is the empirical estimate (mean \pm std over trajectories). All 16 patches agree in sign: both predicted and empirical exponents are negative, so $d_{\text{KY}}^{\text{eff}} = 0$.

patch	R_k	λ_k	Λ_{pred}	$\hat{\Lambda}_k$	std
0	231.7		-0.0552	-0.00496	0.0067
3	181.9		-0.0572	-0.00269	0.0068
12	184.8		-0.0587	-0.00399	0.0064
4	176.1		-0.0656	-0.00809	0.0067
8	174.1		-0.0639	-0.00666	0.0087
15	156.7		-0.0625	-0.00419	0.0068
7	137.7		-0.0687	-0.00672	0.0054
11	138.3		-0.0699	-0.00746	0.0059
1	93.7		-0.0783	-0.00838	0.0060
2	93.3		-0.0777	-0.00759	0.0054
13	72.4		-0.0860	-0.00895	0.0054
14	65.5		-0.0875	-0.00883	0.0042
6	53.6		-0.0961	-0.01126	0.0048
10	41.7		-0.1006	-0.01098	0.0058
5	42.7		-0.1012	-0.01148	0.0052
9	38.7		-0.1055	-0.01248	0.0056

The CelebA-HQ result provides the complementary case to CIFAR-10. On CIFAR-10, patch variances are small ($\lambda_k \ll \lambda^{**}$ for 8×8 patches), so the Gaussian baseline predicts no expansion and the empirically observed Regime II crossover is entirely driven by non-Gaussian score corrections; the suppression-corrected formula reduces to the CIFAR-10 case by continuity. On CelebA-HQ with 16×16 patches, patch variances far exceed λ^{**} and the Gaussian baseline predicts strong expansion, but the measured directional suppression field is large enough to suppress all patches below the corrected threshold: $\lambda^{***} = 500 \gg \lambda_{\text{max}} = 231.7$. In both cases the suppression-corrected formula of Theorem 27 gives the correct sign prediction for every patch, and the two experiments together span the full range of the theory’s applicability: CIFAR-10 tests the regime where $\lambda_k < \lambda^{**}$ and suppression is irrelevant to the sign (though it modifies the magnitude), while CelebA-HQ tests the regime where $\lambda_k \gg \lambda^{**}$ and suppression is the only mechanism preventing $d_{\text{KY}}^{\text{eff}} > 0$.

8 Conclusion

The paper answers how a discrete denoising chain Φ assembles global spatial context early and synthesises local fine detail late, and why self-attention is the natural architectural primitive for this process. The key lies in proving that the DDIM reverse chain is a PIFS whose geometry is governed by three computable quantities derived entirely from the noise schedule and patch covariance spectrum.

The contraction threshold L_t^* sets the minimum score gain required for a contractive step. It depends only on the schedule and carries no dependence on the network or the data. The per-step diagonal expansion function $f_t(\lambda)$ determines when each patch’s own Jacobian block expands. The directional suppression field $S_{k,t}$ measures how strongly the trained score counteracts that expansion. Together they produce the known two-regime structure. Throughout Regime I the directional suppression field keeps every diagonal block below an expansion threshold, while diffuse attention maintains strong cross-patch coupling. In Regime II attention localises as suppression is released patch by patch in variance order. The Regime I/II transition aligns with the spontaneous symmetry breaking reported by Raya and Ambrogioni (2023).

Score-matching training connects to the PIFS structure through an analogue of the Collage Theorem. The denoising objective is, up to timestep reweighing, the diffusion analogue of Barnsley’s collage error. Minimising it not only pulls individual trajectories toward the PIFS fixed point but controls the Wasserstein-1 distance from the prior to that fixed point at a rate proportional to the square root of the excess score risk. The proposed PIFS regulariser enforces the block-max contraction condition (PC) directly during training, provably widening the contraction margin.

The attractor dimension is governed by a discrete Moran equation $\prod_t f_t(\lambda^{**}) = 1$. A patch contributes to sample diversity if and only if its leading variance exceeds λ^{**} . The suppression-corrected Kaplan-Yorke formula quantifies how the learned score reduces attractor dimension below the Gaussian baseline, and the proportionality between information gain and KY dimension growth links schedule design to diversity control.

The PIFS framework leads to the contraction threshold L_t^* , the per-step diagonal expansion function $f_t(\lambda)$ and the global expansion threshold λ^{**} which require no model evaluation. They lead to three design criteria, which allow us to explain existing empirical design choices: the Nichol and Dhariwal (2021) cosine offset, the Hoogeboom et al. (2023) resolution shift, Min-SNR weighting (Hang et al., 2023) and the Align Your Steps schedule (Sabour et al., 2024). Next to exploring the practical applications of the framework, of course also several theoretical directions remain open. As all results are stated for the deterministic DDIM sample, a first natural question is whether the theory transfers to the stochastic case.

We conclude that the power of a self-similar patch structure in natural images, which Barnsley identified in 1988, is also the driving force behind the success of denoising diffusion models.

References

- Michael Albergo and Eric Vanden-Eijnden. Building normalizing flows with stochastic interpolants. In *ICLR*, 2023.
- Stefan Banach. Sur les opérations dans les ensembles abstraits et leur application aux équations intégrales. *Fundamenta Mathematicae*, 3:133–181, 1922.
- Michael F. Barnsley. *Fractals Everywhere*. Academic Press, 1988.
- Sitan Chen, Sinho Chewi, Jerry Li, Yuanzhi Li, Adil Salim, and Andrej Risteski. Sampling is as easy as learning the score: theory for diffusion models with minimal assumptions. In *International Conference on Learning Representations (ICLR)*, 2023. URL https://openreview.net/forum?id=S89Zrt9p_S.
- Kenneth J. Falconer. *Fractal Geometry: Mathematical Foundations and Applications*. Wiley, 1990.
- Tiankai Hang, Shuyang Gu, Chen Li, Jianmin Bao, Dong Chen, Han Hu, Xin Geng, and Baining Guo. Efficient diffusion training via Min-SNR weighting strategy. In *ICCV*, 2023.
- Jonathan Ho, Ajay Jain, and Pieter Abbeel. Denoising diffusion probabilistic models. In *Advances in Neural Information Processing Systems*, volume 33, pages 6840–6851, 2020.
- Emiel Hoogeboom, Jonathan Heek, and Tim Salimans. simple diffusion: End-to-end diffusion for high resolution images. In Andreas Krause, Emma Brunskill, Kyunghyun Cho, Barbara Engelhardt, Sivan Sabato, and Jonathan Scarlett, editors, *Proceedings of the 40th International Conference on Machine Learning*, volume 202 of *Proceedings of Machine Learning Research*, pages 13213–13232. PMLR, 23–29 Jul 2023. URL <https://proceedings.mlr.press/v202/hoogeboom23a.html>.
- John E. Hutchinson. Fractals and self-similarity. *Indiana University Mathematics Journal*, 30(5):713–747, 1981.
- Aapo Hyvärinen. Estimation of non-normalized statistical models by score matching. *Journal of Machine Learning Research*, 6:695–709, 2005.
- Arnaud E. Jacquin. Image coding based on a fractal theory of iterated contractive image transformations. *IEEE Transactions on Image Processing*, 1(1):18–30, 1992.
- James L. Kaplan and James A. Yorke. Chaotic behavior of multidimensional difference equations. In H.-O. Peitgen and H.-O. Walther, editors, *Functional Differential Equations and Approximation of Fixed Points*, pages 204–227. Springer, Berlin, 1979.
- Diederik P. Kingma, Tim Salimans, Ben Poole, and Jonathan Ho. Variational diffusion models. In M. Ranzato, A. Beygelzimer, Y. Dauphin, P.S. Liang, and J. Wortman Vaughan, editors, *Advances in Neural Information Processing Systems*, volume 34, pages 21696–21707. Curran Associates, Inc., 2021. URL <https://proceedings.neurips.cc/paper/2021/hash/b57888cd510c2830a35d9d2094600650-Abstract.html>.

Yaron Lipman, Ricky T. Q. Chen, Heli Ben-Hamu, Maximilian Nickel, and Matt Le. Flow matching for generative modeling. In *International Conference on Learning Representations*, 2023.

Xingchao Liu, Chenyue Gong, and Qiang Liu. Flow straight and fast: Learning to generate and transfer data with rectified flow. *ICLR*, 2023.

Alexander Quinn Nichol and Prafulla Dhariwal. Improved denoising diffusion probabilistic models. In *International Conference on Machine Learning*, pages 8162–8171, 2021.

William Peebles and Saining Xie. Scalable diffusion models with transformers. In *IEEE International Conference on Computer Vision*, pages 4195–4205, 2023.

Gabriel Raya and Luca Ambrogioni. Spontaneous symmetry breaking in generative diffusion models. *Advances in Neural Information Processing Systems*, 2023.

Amirmojtaba Sabour, Sanja Fidler, and Karsten Kreis. Align your steps: Optimizing sampling schedules in diffusion models. In *Proceedings of the 41st International Conference on Machine Learning*, volume 235 of *Proceedings of Machine Learning Research*, pages 42738–42758. PMLR, 2024. URL <https://proceedings.mlr.press/v235/sabour24a.html>.

Jiaming Song, Chenlin Meng, and Stefano Ermon. Denoising diffusion implicit models. In *International Conference on Learning Representations*, 2021a.

Yang Song, Jascha Sohl-Dickstein, Diederik P. Kingma, Abhishek Kumar, Stefano Ermon, and Ben Poole. Score-based generative modeling through stochastic differential equations. In *International Conference on Learning Representations*, 2021b. arXiv:2011.13456.

Pascal Vincent. A connection between score matching and denoising autoencoders. *Neural Computation*, 23(7):1661–1674, 2011.

Use of AI assistance. During the preparation of this manuscript, the author used a Large Language Model to assist with brainstorming, coding and editing prose for clarity.

Appendix A. Extension to Flow Matching

The patch-local contraction framework extends naturally to flow matching (Lipman et al., 2023; Albergo and Vanden-Eijnden, 2023; Liu et al., 2023). In flow matching, the vector field $v_\theta(x, t)$ is trained to interpolate between noise and data along straight paths, replacing the noise-schedule parameterisation of DDPM/DDIM. The Euler discretisation of the resulting ODE takes the same form as Φ_t with a different coefficient structure, and the fixed point argument carries through under an analogous isotropy property.

Definition 36 ((PC-FM): Patch Contraction for Flow Matching) *The vector field $v_\theta : \mathbb{R}^n \times [0, 1] \rightarrow \mathbb{R}^n$ satisfies (PC-FM) at time t if:*

1. $J_x v_\theta(x, t) = -(\mu_t(x)/(1-t))I_n + R_t(x)$ for all $x \in \mathbb{R}^n$, where $\mu_t : \mathbb{R}^n \rightarrow \mathbb{R}$ satisfies $0 < \mu_t^{\min} \leq \mu_t(x) \leq \mu_t^{\max}$;
2. $\|R_t(x)\|_{\text{op}} \leq \tilde{\delta}_t$ uniformly in x ;
3. $\mu_t^{\min} > \tilde{\delta}_t(1-t)$ (ensures $\tilde{\kappa}_t > 0$) and $\mu_t^{\max} < T(1-t)$ (ensures the Euler coefficient $1 - \mu_t^{\max}/(T(1-t))$ stays non-negative).

Theorem 37 (Flow Matching Fixed Point Theorem) *Suppose (PC-FM) holds at each $t \in \{0, \frac{1}{T}, \dots, \frac{T-1}{T}\}$. The Euler step $\Psi_t : \mathbb{R}^n \rightarrow \mathbb{R}^n$,*

$$\Psi_t(x) := x + \frac{1}{T}v_\theta(x, t),$$

is a contraction on $(\mathbb{R}^n, \|\cdot\|_2)$ with factor

$$\tilde{\kappa}_t := \left(1 - \frac{\mu_t^{\min}}{T(1-t)}\right) + \frac{\tilde{\delta}_t}{T} \in (0, 1). \quad (66)$$

The composition $\Psi := \Psi_{(T-1)/T} \circ \dots \circ \Psi_0 : \mathbb{R}^n \rightarrow \mathbb{R}^n$ has a unique fixed point in $(\mathbb{R}^n, \|\cdot\|_2)$ reached at geometric rate $\tilde{s} := \prod_t \tilde{\kappa}_t < 1$.

Proof Differentiating $\Psi_t(x) = x + \frac{1}{T}v_\theta(x, t)$ and substituting (PC-FM) condition (1):

$$J_x \Psi_t = I + \frac{1}{T}J_x v_\theta = \left(1 - \frac{\mu_t(x)}{T(1-t)}\right)I_n + \frac{R_t(x)}{T}.$$

The scalar coefficient $c_t(x) := 1 - \mu_t(x)/(T(1-t))$ satisfies $0 \leq c_t(x) \leq 1 - \mu_t^{\min}/(T(1-t))$ by conditions (1) and (3). Applying the triangle inequality:

$$\|J_x \Psi_t\|_{\text{op}} \leq c_t(x) + \frac{\tilde{\delta}_t}{T} \leq 1 - \frac{\mu_t^{\min}}{T(1-t)} + \frac{\tilde{\delta}_t}{T} = \tilde{\kappa}_t.$$

The first part of condition (3) ($\mu_t^{\min} > \tilde{\delta}_t(1-t)$) gives $\tilde{\kappa}_t < 1$; combined with $c_t(x) \geq 0$ (from the second part of condition (3)), this gives $\tilde{\kappa}_t > 0$. We get that $\|\Psi_t(x) - \Psi_t(y)\|_2 \leq \tilde{\kappa}_t \|x - y\|_2$. Composing over t and applying Theorem 4 completes the proof. Near $t = 1$, $\tilde{\kappa}_t \rightarrow 0$, consistent with the sharp convergence of flow matching at the clean-data end. ■

Notation Summary

Symbol	Meaning
<i>Forward process and schedule</i>	
$x_0 \in \mathbb{R}^n$	Clean image
$x_t \in \mathbb{R}^n$	Noisy image at timestep t
$\bar{\alpha}_t$	Cumulative noise schedule coefficient
$v_t = 1 - \bar{\alpha}_t$	Residual noise variance at step t
$\text{SNR}_t = \bar{\alpha}_t/v_t$	Signal-to-noise ratio at step t
<i>Denoising operator</i>	
$\hat{\varepsilon}_\theta(x_t, t)$	Learned noise-prediction network
$\varepsilon_\theta^*(x_t, t) = -\sqrt{v_t}\nabla_{x_t} \log p_t$	True (Bayes-optimal) score
$\hat{x}_0(x_t, t)$	Predicted clean image
Φ_t	Single-step DDIM operator (4)
$\Phi = \Phi_1 \circ \dots \circ \Phi_T$	Full reverse chain
b_t	Score step coefficient (5)
$\Delta_t(x) = \hat{\varepsilon}_\theta(x, t) - \varepsilon_\theta^N(x, t)$	Per-step deviation field (28)
$\hat{\Delta}_t(x_0, \varepsilon) = \hat{\varepsilon}_\theta(x_t^{\text{real}}, t) - \hat{\varepsilon}_\theta(x_t^{\text{noise}}, t)$	Paired-difference proxy for Δ_t (65)
<i>Euclidean contraction (EC)</i>	
L_t^*	Contraction threshold, schedule-only (10)
$\nu_t(x), \nu_t^{\min}$	Isotropic score coefficient and its infimum (9)
$R_t(x), \delta_t$	Jacobian residual and its operator-norm bound (9)
κ_t, s	Per-step and global (EC) contraction factors (13)
$\mathcal{R}_t(x_t)$	Schedule-geometry displacement under true score (22)
<i>Block-max contraction (PC)</i>	
$\ \cdot\ _{\infty, M}$	Block-max norm $\max_k \ x^{(k)}\ _2$ (17)
$\mathcal{C}_{k,t}(x)$	Score-coupling field $ b_t \sum_{j \neq k} \ [J_x \hat{\varepsilon}_\theta]_{kj}\ _{\text{op}}$ (16)
$\kappa_t^{\text{diag}}, \delta_t^{\text{cross}}$	Diagonal block norm and cross-patch coupling, (PC) (19)
$\kappa_t^{\text{pc}} = \kappa_t^{\text{diag}} + \delta_t^{\text{cross}}$	Per-step (PC) contraction factor (19)
$s^{\text{loc}} = \prod_t \kappa_t^{\text{pc}}$	Global (PC) contraction factor
<i>Regime structure and suppression</i>	
$\lambda_k = \ \Sigma_k\ _{\text{op}}$	Leading eigenvalue of patch k covariance
$f_t(\lambda)$	Per-step diagonal expansion function (26)
$\lambda^*(t)$	Per-step expansion threshold (27)
$S_{k,t}(x), \gamma_{k,t}(x)$	Directional suppression field and suppression margin (30)–(31)
t_k^{rel}	Per-patch release time (33)

<i>Attractor geometry</i>	
ℓ_i	Lyapunov exponents of Φ at fixed point (43)
$\Lambda(\mu) = \frac{1}{T} \sum_t \log f_t(\mu)$	Mean log-expansion rate at spectral value μ
λ^{**}	Global Moran expansion threshold ($\prod_t f_t(\lambda^{**}) = 1$) (45)
$d_{KY}(\mathcal{A})$	Kaplan-Yorke dimension (44)
$g_{k,t} = f_t(\lambda_k) - S_{k,t}(x_t)$	Suppression-corrected diagonal factor, evaluated along $x_t \sim q(x_t)$ (48)
$\Lambda_{\text{eff},k} = \frac{1}{T} \sum_t \mathbb{E}_{x_t}[\log g_{k,t}]$	Suppression-corrected Lyapunov exponent (49)
$d_{KY}^{\text{eff}}(\mathcal{A})$	Suppression-corrected Kaplan-Yorke dimension (50)
<hr/>	
<i>Collage / distributional quantities</i>	
\mathcal{H}	Hutchinson operator $\mathcal{H}(A) = \bigcup_i w_i(A)$ on compact sets (6)
d_H	Hausdorff metric on $\mathcal{K}(X)$ (6)
$\mathcal{W}_1(\mu, \nu)$	Wasserstein-1 distance between probability measures
$\mathcal{W}_2(\mu, \nu)$	Wasserstein-2 distance between probability measures
